Applied Thermal Engineering 278 (2025) 127230

Contents lists available at ScienceDirect

Applied Thermal Engineering

journal homepage: www.elsevier.com/locate/ate

Research Paper

Dynamic thermal performance and management analysis for a 48 V lithium-ion battery pack under real-world driving conditions

Hossein Darvish, Antonio Paolo Carlucci *, Domenico Laforgia

Department of Engineering for Innovation, University of Salento, Via Per Monteroni, Lecce, 73100, Italy

ARTICLE INFO

Keywords:
Lithium-ion battery
Electric vehicle
Battery temperature
Temperature prediction
Cooling system

ABSTRACT

This study investigates the thermal behavior of a 48 V lithium-ion battery (LIB) pack under dynamic operating conditions using experimental and numerical methods. While most existing research targets high-voltage systems or steady-state scenarios, this work addresses the overlooked case of low-voltage packs under real-world transient loads. An indirect liquid cooling mechanism was utilized, activating at approximately 40 °C. Five test cases were examined: a full charge-discharge cycle (Case 1), worldwide harmonized light duty test cycle (WLTC) profiles and their inverted versions at initial state of charge (SOC) levels of approximately 90% and 60% (Cases 2 and 3), and the effects of initial temperature and temperature difference, the difference between the highest and lowest temperature points within the pack (Cases 4 and 5). Thermal behavior was analyzed at cell, module, and pack levels using 27 thermocouples, whose utilization is rarely documented in literature. A sensitivity analysis identified the specific heat and density of the cells as key parameters influencing thermal predictions, highlighting the importance of precise thermophysical characterization. Results indicated temperature variation across modules, influenced by cooling strategy. Maximum temperature rises during WLTC driving cycles were 10.5 °C, 11.4 °C, and 9.1 °C for Cases 2, 3, and 4, respectively, highlighting the influence of initial SOC and temperature. Although the initial temperature difference did not affect temperature rise, it influenced temperature gradients (Case 5). The indirect liquid cooling system effectively maintained pack temperatures below 40 °C under WLTC and inverted conditions, while constant high-current cycling led to higher peaks around 46 °C. These findings underscore the complexity of thermal management in LIB packs under dynamic conditions and emphasize the effectiveness of indirect liquid cooling in limiting temperature rise. This work offers practical insights for optimizing alternative battery thermal management strategies in electric vehicle applications.

1. Introduction

In recent decades, the global challenges of energy resource shortage and climate change due to fossil fuel use have arisen. The transportation sector, being one of the largest consumers of fossil fuels, is a significant contributor to these issues [1,2]. As a result, the automotive industry is shifting towards clean energy technologies. Among different technologies, electric vehicles (EVs) and hybrid electric vehicles (HEVs) stand out for their higher efficiency, reduced emissions, lower noise, and regenerative braking capabilities [3].

Forecasts indicate that HEVs are expected to account for 36% of the market by 2030 [4]. Within this category, 48 V mild hybrid electric vehicles (MHEVs) are particularly promising for reducing both CO_2 emissions and vehicle production costs [5,6]. This shift towards EVs places increasing demands on energy storage systems, particularly lithium-ion batteries (LIBs), whose performance and safety are closely tied to effective thermal management.

LIB cells, the core component in EVs, have attracted significant research interest. Compared to other types of energy storage [7–9], LIB cells are preferred in new energy vehicles due to their long service life, low self-discharge rate, and high power and energy densities [10,11]. However, the cycle life, performance, and safety of LIB cells are highly dependent on their operating temperature [1,2,12–16]. The optimal temperature range for LIB cells is between 15 °C and 35 °C, with a maximum temperature difference of less than 5 °C between modules in a battery pack to ensure optimal performance and longevity [1,2,17–20].

To maintain LIB cell temperatures within the optimal range and minimize temperature difference between cells, a battery thermal management system (BTMS) is crucial [21,22]. BTMSs can be categorized into various types, such as active or passive, series or parallel (a definition of series, *s*, and parallel, *p*, connections of battery cells is provided in Section 2.2), heating or cooling, internal or external, air or

* Corresponding author.
E-mail addresses: hossein.darvish@unisalento.it (H. Darvish), paolo.carlucci@unisalento.it (A.P. Carlucci), domenico.laforgia@unisalento.it (D. Laforgia).

https://doi.org/10.1016/j.applthermaleng.2025.127230
Received 14 January 2025; Received in revised form 9 June 2025; Accepted 14 June 2025
Available online 6 July 2025

Nomenclature

Acronyms

BMS	battery management system
BTMS	battery thermal management system
C	charge period
D	discharge period
DOD	depth of discharge
EV	electric vehicle
ExH	extra high
H	high
HEV	hybrid electric vehicle
L	low
LIB	lithium-ion battery
M	medium
MAE	mean absolute error
MHEV	mild hybrid electric vehicle
NCM	lithium nickel manganese cobalt oxide
NTGK	Newman, Tiedemann, Gu, and Kim
OFAT	one factor at a time
PCM	phase change material
RMSE	root mean square error
SOC	state of charge
WLTC	worldwide harmonized light duty test cycle

Dimensionless Numbers

Ra_L	Rayleigh number

Symbols

$\Delta T(t)$	temperature difference (°C)
$\Delta T_l(t)$	coolant temperature difference (°C)
ρ_b	density ($kg\,m^{-3}$)
A	surface area (m^2)
c_{pb}	specific heat capacity ($J\,kg^{-1}\,K^{-1}$)
h	convection heat transfer coefficient ($W\,m^{-2}\,K^{-1}$)
I_{max}	maximum current (A)
I_{min}	minimum current (A)
I_{pack}	pack current (A)
k_b	battery thermal conductivity ($W\,m^{-1}\,K^{-1}$)
k_f	thermal conductivity of gap (g) or bottom plate (p) ($W\,m^{-1}\,K^{-1}$)
k_g	gap thermal conductivity ($W\,m^{-1}\,K^{-1}$)
k_p	bottom plate thermal conductivity ($W\,m^{-1}\,K^{-1}$)
k_w	thermal conductivity of battery (b) or bottom plate (p) ($W\,m^{-1}\,K^{-1}$)
$LiNiMnCoO_2$	lithium nickel manganese cobalt oxide
n	denotes the direction
q_{gen}	total heat generation ($W\,m^{-3}$)
SOC_i	initial state of charge (%)
SOC_{pack}	pack state of charge (%)
T_a	ambient temperature (°C)
$T_{avg}(t)$	average temperature (°C)
$T_{avg,Module1}(t)$	average temperature of Module1 (°C)
$T_{avg,Module2}(t)$	average temperature of Module2 (°C)
$T_{avg,Module3}(t)$	average temperature of Module3 (°C)
$T_{avg,Pack}(t)$	average pack temperature (°C)
T_i	initial temperature (°C)
$T_{l,i}(t)$	inlet coolant temperature (°C)
$T^z_{m,c}(t)$	thermocouple position name (°C)
$T_{min}(t)$	minimum temperature (°C)
$T_{max}(t)$	maximum temperature (°C)
$T_{o,i}(t)$	outlet coolant temperature (°C)
T_{rise}	temperature rise (°C)
$T_{s,n}$	outer surface temperature (°C)
V_{pack}	pack voltage (V)

Subscripts/superscripts

+	close to the positive tab
−	close to the negative tab
a	ambient
avg	average
$avg, Module1$	average Module1
$avg, Module2$	average Module2
$avg, Module3$	average Module3
$avg, Pack$	average pack
b	battery
c	cell number (in the range of 01 to 12)
f	either g or p
g	gap
gen	generation
i	initial state of charge or temperature
j	thermocouple position (m, z)
l	liqui
l, i	liquid, inlet
l, o	liquid, outlet
L	Rayleigh number subscript
m	module number (1, 2, or 3)
n	denotes the direction
p	bottom plate/specific heat capacity subscript
$rise$	rise
s	surface
w	either b or p
z	either − or +, represents the negative or positive tab, respectively

liquid or phase change material (PCM), or hybrid strategies combining multiple methods [1,2,23]. Each type possesses its advantages and disadvantages, and the choice depends on factors such as volumetric constraints, installation costs, and efficiency. Modern EVs and HEVs typically use active methods. Liquid cooling systems, due to their higher thermal conductivity and specific heat capacity compared to air, provide better thermal performance and cooling efficiency [1,2,24]. The liquid cooling system can be used either directly or indirectly in contact with the coolant and battery surface.

Experiments on the thermal behavior of MHEV LIBs have been performed on both individual cells and packs, with and without the implementation of cooling systems. However, a detailed analysis of how external factors, such as the presence of other cells and real-time operational profiles, affect the internal temperature distribution remain limited [25,26]. High-resolution thermal analysis of LIB packs under realistic operating conditions is needed to enhance the development of effective and reliable thermal management systems.

Research on the thermal behavior of 48 V LIB packs is limited. For instance, Lee et al. studied a 0.4 kW, 48 V, 8 Ah LIB pack designed for an MHEV used in ground transportation [5]. Their work involved monitoring overall temperature, current, and voltage during three driving cycles. They observed that the battery pack temperature, recorded at a single location, increased by approximately 6.0 °C during each driving cycle. However, their study did not investigate temperature distribution among individual cells or provide specific details about LIB cell dimensions or thermocouple placement.

Similarly, Hall et al. examined the design challenges of a 48 V MHEV battery pack, focusing on cell selection and thermal performance [27]. Using 18 LIB cells connected in series, they observed an 11.0 °C temperature rise following a full charge or discharge event but did not study temperature distribution within the pack.

Anselma et al. explored a BTMS control framework for a 48 V LIB pack in a $14s11p$ configuration (meaning that 14 cells are connected in series to increase voltage, and 11 sets of these three series cells are connected in parallel to increase capacity) for a HEV powertrain, analyzing temperature-unaware, battery current-constrained, and temperature-constrained strategies [28]. Their findings indicated the temperature-aware strategy was superior in energy consumption and fuel savings, especially at higher ambient temperatures. However, they did not consider varying initial state of charges (SOCs), internal temperature differences, or different driving scenarios.

In summary, previous experimental studies on MHEVs have primarily focused on the performance of LIB cells, modules, and packs using a limited number of thermocouples to monitor pack thermal behavior under various cooling strategies and both steady-state and dynamic conditions. Real MHEV battery packs experience irregular currents under mixed charging and discharging processes, making steady-state conditions insufficient to represent actual phenomena [29]. Even dynamic condition studies have not applied high currents to LIB packs [20], and many rely on current and power profiles from previous literature rather than real scenarios. As a result, there is a lack of detailed temperature distribution studies in LIB packs for automotive applications under real operational conditions.

This study aims to fill the gap in existing research by examining the thermal performance of a 48 V LIB pack designed for an MHEV, incorporating an indirect liquid cooling system. To better replicate actual driving conditions, besides fully charging and discharging cycles, the worldwide harmonized light duty test cycle (WLTC) – a standardized driving cycle that simulates diverse speed profiles and introduces realistic and high-current load patterns, unlike the simplified or averaged profiles commonly used in previous studies – is used as a benchmark. In addition, 25 temperature sensors – whose utilization is rarely documented in literature – are strategically positioned within the LIB pack to provide a detailed temperature distribution across cells and modules, enabling a comprehensive thermal analysis. Furthermore, the effect of initial temperature gradients (i.e., the difference between the highest and lowest initial temperature points within the pack, a parameter that has not been previously explored) is examined. Finally, the performance of the indirect liquid cooling system is studied through numerical simulations and experimental monitoring of the inlet and outlet coolant temperatures.

In previous works by the same authors [30–32], several key aspects of LIB pack thermal behavior were explored. The current work integrates and expands upon these studies by introducing three significant advancements:

- Examining the impact of initial temperature differences on thermal distribution using real-world driving cycles.
- Investigating the effectiveness of an indirect liquid cooling system in managing LIB pack temperatures exceeding the maximum threshold through numerical and experimental methods.
- Comparing temperature distribution and cooling system performance during dynamic cycling and fully charged-discharge cycles.

Table 1
Key characteristics of the LIB cells and pack utilized in this study.

Parameter	Unit	Cell value	Pack value
Shape type	–	Prismatic	$12s3p$
Chemistry	–	NCM	NCM
Nominal capacity	Ah	8.23	24.69
Nominal voltage	V	3.7	44.4
Maximum voltage	V	4.17	50
Maximum current	A	233	700
Dimensions (length × width × height)	mm	144 × 17 × 60	660 × 475 × 132

The rest of this paper is organized as follows: Section 2 provides an overview of the experimental setup, LIB cell and pack parameters, the indirect liquid cooling system, tested operating conditions, and the theoretical background of the numerical simulation. Section 3 presents the validation and verification of the numerical simulation, along with a sensitivity analysis. This section is followed by analysis of the results derived from SOCs, temperature measurements, average temperature, and temperature differences between battery cells, modules, and the pack for all cases, as well as the performance of the liquid cooling system. The results are discussed in Section 4. Finally, conclusions and suggestions for future research are presented in Section 5.

2. Materials and methods

This section introduces LIB cells and parameters of the 48 V pack. The designed experimental layout is then presented, illustrating the charging-discharging architecture setup with the liquid cooling system. Additionally, different cases are introduced, explaining the appropriate initial and boundary conditions. Furthermore, sensitivity analysis approach used in this study is presented in details. Eventually, the numerical procedure for simulating a LIB cell is described.

2.1. Lithium-ion battery cell parameters

LIB cells are composed of positive and negative electrodes, electrolytes, separators, and current collectors [23]. In the automotive sector, prismatic, pouch, and cylindrical shaped battery cells are widely utilized [33–35]. Each of these cell formats presents specific trade-offs [36–38]. Cylindrical cells offer strong mechanical stability and ease of manufacturing; however, they are characterized by lower space efficiency. Prismatic cells provide high energy density and high packing efficiency, although they are more complex and costly to manufacture. Pouch cells deliver the highest flexibility and energy density; nevertheless, they are more prone to swelling and require additional structural support. In this study, prismatic cells were selected for their balance of space utilization, structural integrity, and energy density, making them suitable for 48 V MHEV applications.

In the EV battery industry, the adoption of lithium nickel manganese cobalt oxide (NCM) batteries, $LiNiMnCoO_2$, has been increasing [39]. NCM batteries are well-regarded for their high C-rate capability during charge and discharge, long lifespan, and good performance at low temperatures [40]. Therefore, NCM LIB cells are utilized in this study. Each LIB cell features a nominal voltage of 3.7 V and a capacity of 8.23 Ah. Table 1 summarizes the electrical and geometrical characteristics of the LIB cells used in this study.

2.2. Lithium-ion battery pack parameters

The thermal performance of a real 48 V LIB pack, equipped with a cooling system, for application in an MHEV is investigated in this study. The selection of a 48 V LIB pack is driven by its ease of integration into an MHEV, minimal impact on overall vehicle weight, safe and compact modular design, and cost-effective contribution to improved fuel efficiency. The battery pack comprises multiple individual cells connected in series and parallel configurations to enhance voltage and

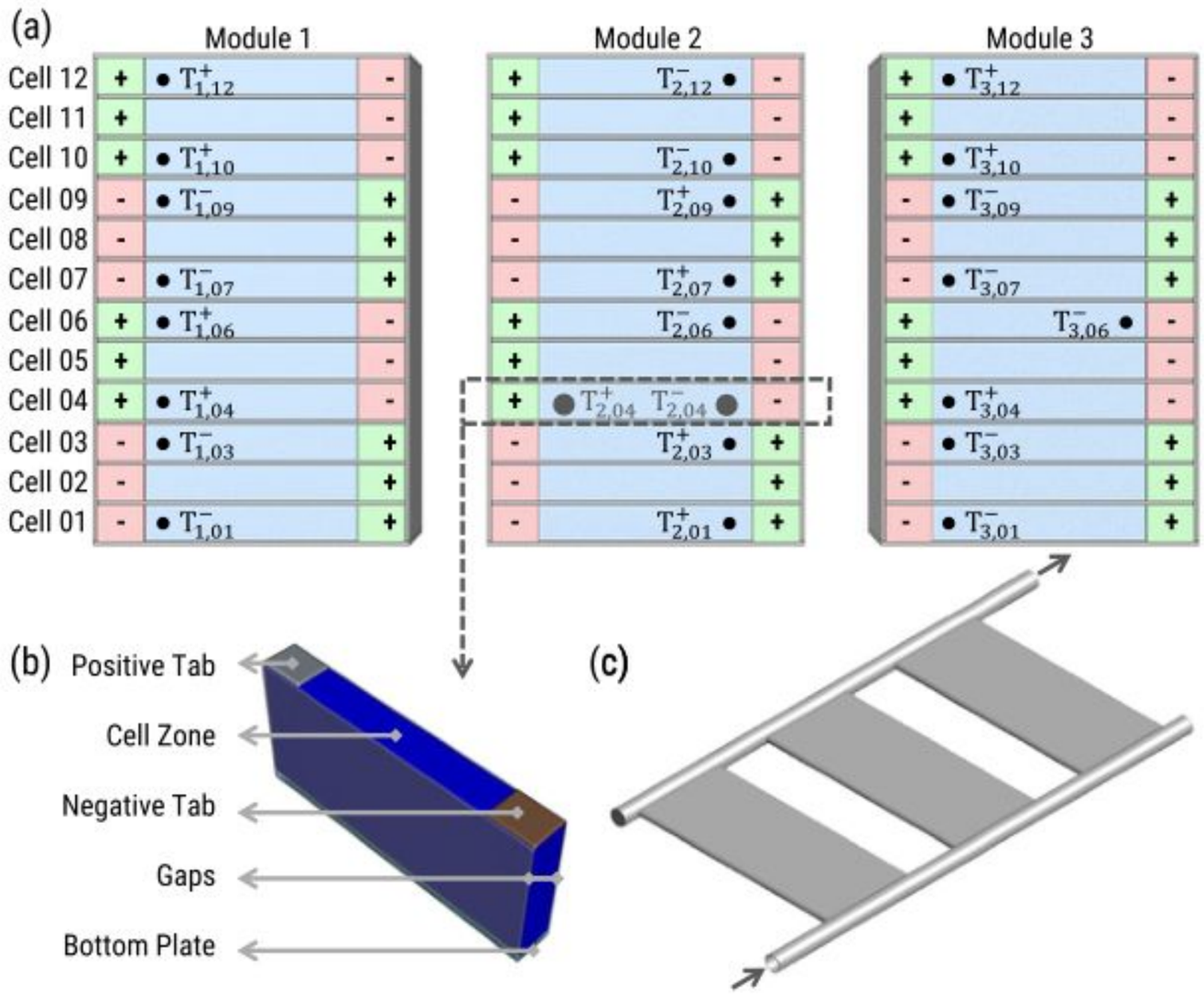

Fig. 1. (a) A top view of the battery pack model showing thermocouple positions and naming convention ($T^{z}_{m,c}$, where m = module number, c = cell number, z = positive/negative tab) in Module1, Module2, and Module3; (b) a 3D view of the battery cell components; (c) an isometric view of the indirect liquid cooling system located at the base of the pack, illustrating relative placement and flow direction. Note: Component sizes are not to scale.

capacity, respectively. The LIB pack utilized in this study aligns with previous works by the same authors [30–32]. A $12s3p$ configuration is used, indicating that three cells are connected in parallel, and 12 groups of these parallel-connected cells are arranged in series. Table 1 outlines the properties of the battery pack used in this study, and Fig. 1 illustrates the structure of the pack, its modules, and individual cells. The LIB cells are separated by thin thermal barriers.

The LIB pack includes various components, such as a battery management system (BMS) circuit, electrical elements like a shunt and a relay, and an aluminum chassis. These specific elements were not replicated in this study due to their structural complexity and the diverse materials involved. The assembly is encased within a metallic sheet, with its dimensions detailed in Table 1.

2.3. Liquid cooling system

A uniform indirect liquid cooling system is implemented at the base of the three modules once the pack reaches a threshold temperature of approximately 40 °C. The schematic layout of the system components is shown in Fig. 2, while Fig. 1c provides a 3D schematic of the cold plate integration beneath the pack. Figs. 1c and 2 reflect the layout and flow paths relevant to the thermal analysis. The cooling system incorporates two tubes (inlet and outlet) to the channels positioned at the base of the modules.

Different heat transfer fluids, including water, deionized water, ethylene glycol-water mixtures, mineral oil, and liquid metal, are explored in the context of both direct and indirect liquid-based cooling systems [24]. The liquid cooling system employed in this study utilizes a mixture of water and ethylene glycol.

The cooling system status can be divided into two distinct phases based on its operation: passive, during which the cooling system is filled with non-circulating liquid; active, during which the liquid circulates (when the temperature threshold is reached).

2.4. Experimental layout

Fig. 2 illustrates the experimental test set-up used in this study. This setup closely follows the configuration presented in previous works by the same authors [30–32]. The main components in the experimental set-up are as follows:

- a battery pack equipped with a BMS;
- an AVL battery bidirectional power supply controlled by the AVL PUMA system;
- 27 K-type temperature sensors (commonly used for their wide temperature range and fast response time) connected to two data acquisition modules (ES620 ETAS);
- a liquid cooling system; and
- a computer unit for data monitoring and storage.

Out of 27 thermocouples, 25 are used to measure the temperature of the LIB cells. As shown in Fig. 1a, the thermocouples are positioned on top of the cells using tape for secure attachment and accurate temperature measurement. The thermocouples are positioned across three modules of the battery pack, named Module1, Module2, and Module3. The labeling convention for the measurement points is defined in Eq. (1).

$$\mathbf{T}_{j}(t) = \mathbf{T}^{z}_{m,c}(t) \tag{1}$$

where m is the module number (1, 2, or 3), c indicates the cell number from 01 to 12, and the superscript z, either − or +, represents the negative or positive tab, respectively. The tabs refer to the thin metal strips attached to the electrodes inside the battery cell, which allow electrons to flow between the electrodes and the external circuit.

In Module1, the thermocouples are placed on the left side, close to the external surface of the pack, to monitor its thermal response to environmental conditions. On the other hand, in Module3, the thermocouples are positioned internally, near Module2, to observe the interactions between the two modules. Additionally, Module3 features an externally positioned thermocouple, $T^{-}_{3,06}$, to evaluate the temperature difference between the external surface of the pack and the internal surface of the module.

The highest temperature in LIB cells typically occurs near the tabs [1,2,41]. In this study, $T^{+}_{2,04}$ and $T^{-}_{2,04}$ are positioned close to the positive and negative tabs of the same cell, respectively (Fig. 1a).

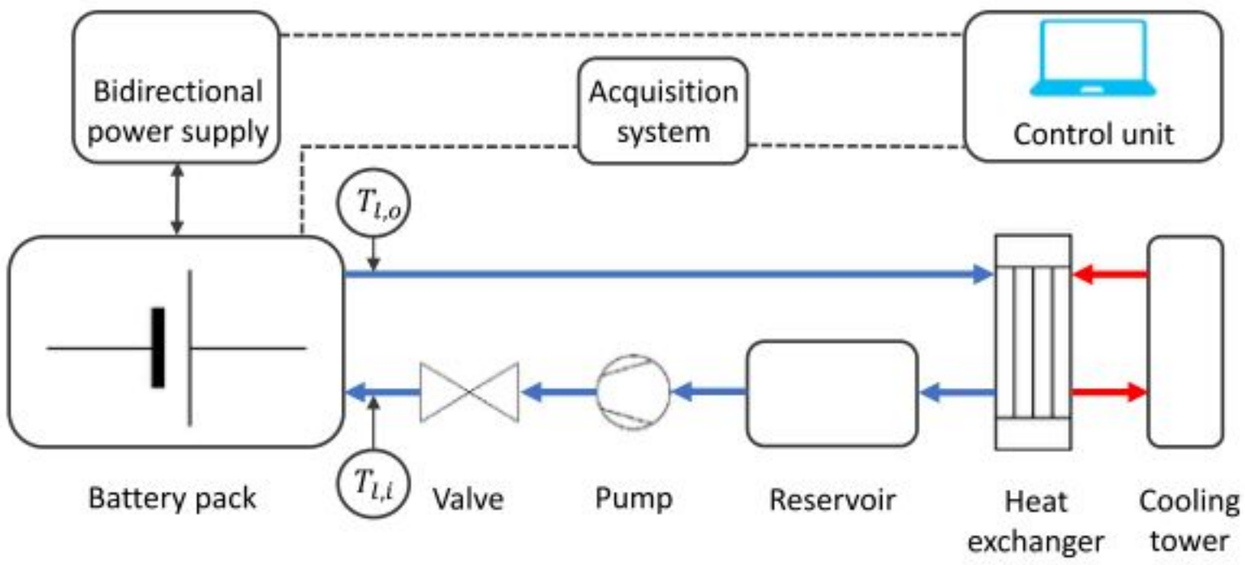

Fig. 2. A schematic of the LIB pack thermal performance test and cooling system used in this study. The inlet and outlet coolant temperatures are denoted as $T_{l,i}$ and $T_{l,o}$, respectively.

Table 2
A summary of the five cases evaluated in this study, including initial temperature, initial state of charge, maximum and minimum current values, test duration, and cycle profile shape. These values define the initial conditions used in the numerical simulations.

Case number	T_i (°C)	SOC_i (%)	ΔT_i (°C)	I_{max} (A)	I_{min} (A)	Time (s)	Shape
Case1	26.2	47	–	237	−237	5180	Fully charge/discharge
Case2	24.0	90	–	600	−600	3600	WLTC & inverted
Case3	24.0	60	–	600	−600	3600	WLTC & inverted
Case4	28.5	92.5	–	600	−600	1800	WLTC
Case5	28.5	90.5	2	600	−600	1800	WLTC

These thermocouples are used to measure the temperature differences between the positive and negative tabs of the same LIB cell during charge and discharge cycles.

The finalized experimental campaign analysis of the thermal performance and the cooling system of the battery pack was carried out at the "Center for Studies of Vehicle Components S.p.A", Bosch plant in Modugno, Bari, Italy.

2.5. Charging and discharging cycles

In the present study, two test protocols – continues full charging-discharging cycles and dynamic charging-discharging cycles determined by the WLTC Class 3b followed by an inverted version of the same cycle – were implemented in order to study the temperature distribution and cooling system effectiveness of the 48 V LIB pack of an MHEV. As shown in Table 2, there are totally five cases with different initial conditions and charging-discharging cycles. In Table 2, T_i, SOC_i, ΔT_i, I_{max}, I_{min}, time, and shape represent the initial temperature, initial SOC, initial temperature difference between the maximum and minimum values within the pack, maximum current, minimum current, test duration, and the shape of the charging and discharging profiles, respectively.

In this study, high charge-discharge currents were selected to simulate the high-power demands of MHEVs, particularly during acceleration and regenerative braking. For dynamic cases (Cases 2–5), a peak current of 600 A was applied over short durations to evaluate the thermal behavior and cooling system response under transient, high-load conditions. In Case1, a peak current of 237 A was employed over extended charging-discharging cycles. This choice reflects practical limitations: applying high currents continuously may lead to excessive heat generation, accelerated aging, and performance degradation of the battery.

The following lines present a description of each case along with the reasoning behind its selection.

- **Case1 (continuous operation with cycling):** In the first case, a series of five full charge-discharge cycle tests was performed, starting at a T_i and SOC_i of 26.2 °C and 47%, respectively. Throughout the cycles, the battery pack experienced maximum and minimum currents of 237 A and −237 A, respectively, while the SOC ranged from 10% to 91%. The test was concluded when the SOC reached its maximum value at the end of the fifth cycle. These cycles were used to study the thermal behavior of the battery pack under varying SOC conditions during both charging and discharging.
  This setup was designed to evaluate thermal behavior under sustained high-current operation, providing a baseline for comparison with dynamic WLTC cases. The extended duration of this case allowed for the activation of the cooling system, enabling the observation of its impact on thermal performance. Therefore, this scenario characterizes the thermal response of the LIB pack under prolonged cycling conditions.
- **Case2 and Case3 (WLTC cycles and inverted):** In these cases, the effect of WLTC Class 3b, followed by an inverted version of the same cycle, on temperature distribution and the cooling system was analyzed. Charging and discharging cycles were conducted with a T_i of 24.0 °C (ambient temperature) and a maximum SOC_i of 90%, defining Case2 in this study. To investigate the influence of different SOC_is, Case3 was derived from Case2 by maintaining the same T_i and lowering the SOC_i to 60%. Prior to each test, the pack was charged or discharged to a specific SOC. This procedure ensured that all test cases began with a specific SOC for consistent and repeatable results.
  It is essential to note that the extended duration of an inverted WLTC in Case2 and Case3 allowed for the activation of the cooling system, facilitating the observation of its impact on thermal performance.
- **Case4 and Case5 (WLTC cycles):** In these cases, the effect of different T_i and ΔT_i (the ΔT is the difference between the maximum and minimum temperatures at each time) during a WLTC Class 3b on temperature distribution was analyzed. In Case4, charging and discharging cycles were conducted with a T_i of 28.5 °C and a high SOC_i of 92.5%. In Case5, the T_i was identical to that of Case4; however, the ΔT_i was set to 2 °C, and the SOC_i was reduced to 90.5%.

2.6. Mathematical battery model and governing equations

To assess the impact of liquid cooling on system thermal behavior under high temperatures, it is imperative to obtain battery temperature

data in the absence of any cooling intervention. Due to safety considerations, the battery pack cannot be subjected to temperatures exceeding a threshold value (40 °C) during testing. Consequently, the utilization of a LIB thermal model becomes essential.

In this investigation, a single LIB cell is selected to evaluate the effectiveness of the liquid cooling system. This decision is motivated by two factors: firstly, the consistency of temperature patterns induced by the cooling system across various cells (as demonstrated in Section 3); and secondly, the desire to minimize computational cost.

It is worth mentioning that the high number of thermocouples in the experimental setup, as mentioned previously, allows us to capture the detailed thermal behavior of the entire LIB battery pack both in the absence and presence of the liquid cooling system. However, for the specific purpose of assessing the performance of the cooling system in reducing temperature rise, analyzing the temperature behavior at a single and strategically selected point (cell $T_{2,04}$) is sufficient. This part provides a reliable indication of the cooling effectiveness, without the need for full pack-level thermal simulations.

As specified in Fig. 1, cell $T_{2,04}$ is chosen for modeling purposes due to its location in the middle of the module, where higher temperatures are typically evident, and to the presence of nearly symmetric boundary conditions.

2.6.1. Energy balance and heat generation

In this study, a multi-scale and multi-dimensional electrochemical–thermal model, known as Newman, Tiedemann, Gu, and Kim (NTGK) in the literature, was adopted. The NTGK models the electrochemical behavior of LIB cells by using semi-empirical relationships to describe voltage, current, and heat generation. This model captures both reversible and irreversible thermal effects and accounts for internal resistance heating, making it suitable for coupled thermal-electrical simulations in battery systems [42,43]. A detailed formulation of the NTGK model can be found in [43–45]. The model was implemented under the following assumptions:

- The distance between the two electrodes is considered short, ensuring that the current flow remains perpendicular to them.
- The electrode is treated as an equivalent network comprising electrode material and current collector resistors connected in parallel [42,46].
- The battery cell is treated as a single domain, utilizing a coupled semi-empirical model. The parameters of this model are derived from [42,44].

The continuity of current and Ohm's law were used to derive the equations for potential and current-density distribution within the battery [47]. The Poisson equations for the potentials in the positive and negative electrodes were derived, and the functional relationship for current density was improved by including the polarization of the electrodes [42].

Heat generation, q_{gen}, occurs inside the battery domain due to chemical reactions during charging-discharging and internal resistance. A detailed description of the equations governing the heat generation components inside the battery cell can be found in the literature [43,44]. In this study, the heat generation due to other sources is neglected as they have no significant impact on the total heat generation [44,48].

The conductive equation with the heat source term governs the heat transfer inside the battery cell as follow (energy conservation equation):

$$\frac{\partial}{\partial t}\left(\rho_b c_{pb} T\right) = \nabla \cdot \left(k_b \nabla T\right) + q_{gen} \tag{2}$$

where ρ_b, c_{pb}, and k_b represent the battery's density, specific heat capacity, and thermal conductivity, respectively. These parameters are listed in Table 3.

2.6.2. Boundary and initial conditions

Heat dissipation from a single cell body happens through three main paths:

- **Gaps:** Assuming the air gaps between the cells as an enclosed space, a dimensionless parameter, Rayleigh number (Ra_L), is used to determine the heat transfer mode in the gaps [49–51]. Heat transfer in the air gaps between cells occurs by conduction due to the small thickness of the gaps (2 mm) and the low Rayleigh number ($Ra_L \leq 10^3$), indicating negligible convection. Therefore, the gaps (shown in Fig. 1b) are considered as a solid domain with the thermophysical properties of the air that are listed in Table 3. The following thermal equilibrium condition at the interface of the battery (subscript of b) and the gap (subscript of g), Eq. (3), is written with an assumption of negligible contact resistance.

$$-k_b \frac{\partial T}{\partial n} = -k_f \frac{\partial T}{\partial n} \tag{3}$$

  where, k_f is considered as either k_g or k_p that are the thermal conductivities of the gap or plate, respectively, and n denotes the direction. It is worth mentioning that each of the two gap bodies considered is half of the real gap, 1 mm, and Neumann boundary conditions have been applied on the outside surfaces (a zero heat flux boundary condition).
- **Bottom plate:** At the bottom of the LIB cell, there is a plate in order to transfer the generated heat to the cooling medium (Fig. 1b). This body includes solid plates assumed to be aluminum and cooling fluid. The fluid is considered not moving as this simulation refers to the passive portion of the tests. The total height of the combined layers is approximately 4 mm; however, the detailed internal structure is not fully known. In this study, to reduce the complexity of the structure, the whole body is considered as a solid body with the thermophysical properties of the aluminum and water combined together as listed in Table 3. Therefore, Eq. (3) shows the heat transfer happens between the battery surface and bottom plate (subscript of p).
  It is worth nothing that, the heat transfer to air from the bottom plate at its outer surface is considered to be a free convective heat transfer to the air, i.e.,

$$-k_w \frac{\partial T}{\partial n} = hA\left(T_{s,n} - T_a\right) \tag{4}$$

  where k_w is either k_b or k_p that are the thermal conductivities of battery or bottom plate, respectively, h is convection heat transfer coefficient ($h = 5\ \mathrm{W\,m^{-2}\,K^{-1}}$), A denotes the surface area, $T_{s,n}$ is the outer surface temperature, and T_a shows the ambient temperature.
- **Convection:** Convective heat dissipation to the ambient air from the remaining battery surfaces is considered in this study, while radiative heat dissipation is neglected. This boundary condition is represented in Eq. (4).

For all simulations, the T_i of the battery cell is assumed to be uniform and equal to the T_a at the beginning of each test case. The values of T_i for each case are listed in Table 2. In addition, the SOC_i is set based on experimental inputs and is provided in Table 2. These initial conditions are applied uniformly throughout the LIB domain. Furthermore, it is assumed that the LIB is initially at rest, with no internal heat generation or temperature gradients present prior to the start of the charge-discharge cycle.

2.7. Numerical simulation setup

In this study, a finite volume-based commercial solver ANSYS FLUENT 2023 R2, is employed to solve the governing equations. The governing equations and the details of the battery model employed in the present simulation are already explained in the previous section. The second-order upwind scheme is employed to discretize energy

Table 3
LIB cell, gap, and bottom plate properties used in the numerical simulation of this study.

Parameters	Unit	LIB cell	Positive tab	Negative tab	Gap	Bottom plate
Density (ρ)	kg m^{-3}	2092	2719	8978	1.225	1858.6
Specific heat (c_p)	J kg^{-1} K^{-1}	1400	871	381	1006.43	2526.5
Thermal conductivity (k)	W m^{-1} K^{-1}	18.2	202.4	387.6	0.242	1.196

equation. The convergence criteria and the under-relaxation coefficient for energy are set at 10^{-3} and 1.

The initial depth of discharge (DOD) and reference battery capacity have been modified based on different test cases in this study. The thermophysical properties have been reported previously and the remaining values are considered as default values of the NTGK model in the software.

A hexahedral structured mesh is applied to the computational domain. The average values for element quality and aspect ratio are 0.94 and 1.27, respectively. To establish the reliability of the numerical model, grid and time-step independence studies have been performed. They are reported in Section 3.1.

The numerical simulation presented in this study was designed to represent the thermal behavior of a representative LIB cell during the passive phase. Since there is no fluid motion during this phase, flow regime characterization is not required. This baseline allowed for comparison against experimental results with active liquid cooling engaged, offering insight into the effectiveness of the cooling system under WLTC loads.

2.8. Sensitivity analysis

In this study, a sensitivity analysis is performed to evaluate the influence of key thermophysical parameters on the simulated LIB cell. Sensitivity analysis is a technique used to assess how variations in model input parameters affect the output, helping to identify and exclude parameters that have negligible influence on the results [52–54].

Among various approaches, simulation-based sensitivity analysis is employed, which examines how changes in input parameters influence simulation outputs. This method is particularly useful for capturing nonlinear relationships between inputs and outputs [53].

Simulation-based methods are generally categorized as either local or global. Local methods, such as the one factor at a time (OFAT) approach, vary one parameter at a time while keeping others fixed at their nominal values. This allows for a clear and straightforward assessment of each parameter's individual effect on the model output [53,55].

On the other hand, global methods (including Monte Carlo and variance-based techniques) evaluate sensitivity across the full range of input values and account for interactions between parameters. While global methods are more comprehensive, they are computationally expensive and require parallel computing resources [53,55].

Due to its simplicity and lower computational demand, the OFAT method is adopted in this study. The values used in the sensitivity analysis are listed in Table 3. This analysis helps identify which parameters most significantly impact the model's thermal response, guiding future model calibration and refinement efforts.

3. Results

The results are organized into six parts. Firstly, the numerical approach is validated and verified to ensure the accuracy and reliability of the findings. Next, a sensitivity analysis of the input parameters is conducted to quantitatively evaluate their influence on the thermal response of the model. Subsequently, the SOC and voltage dynamics are examined, focusing on the variations in initial SOCs and their evolution over the test period across the five test cases. Furthermore, a detailed examination of the thermal behavior during full charging and discharging cycles is presented, analyzing the performance of individual cells, modules, and the pack itself in the first test case. Following this, the thermal behavior observed in the remaining four test cases are examined. Finally, the effectiveness of the indirect cooling system on temperature management is explored, providing insights into how the cooling system influences thermal performance of Case1, Case2, and Case3.

3.1. Numerical model validation and verification

This section presents the verification and validation of the numerical model used in this study. Verification aims to ensure that the numerical solution is independent of discretization parameters such as mesh size and time step. Validation, on the other hand, evaluates the accuracy of the model by comparing simulation results with the corresponding experimental results. To examine these independencies, the average temperature, T_{avg}, of the top surface of LIB cell over time is used as the reference temperature under a constant C-rate profile.

For verification, mesh and time step independence studies were conducted using the time-averaged temperature of the selected reference temperature. The relative error, expressed as a percentage, was calculated as the difference between successive mesh results, normalized by the value obtained from the coarser mesh. For validation, the root mean square error (RMSE) and mean absolute error (MAE) were used to quantify the difference between the simulated and experimental results.

- **Grid independence study (verification):** Grid independence is assessed by varying the element size. Mesh domains with approximately 25k, 62k, 193k, and 473k elements are considered (Fig. 3a). Results indicate negligible differences in T_{avg} between the 193k and 473k meshes, with relative errors of 0.10% between the 62k and 193k meshes, and 0.03% between the 193k and 473k meshes. Therefore, the 193k mesh is selected for further studies.
- **Time step independence study (verification):** Larger time steps yield faster results but with greater inaccuracies, while smaller time steps improve accuracy at the cost of increased computational time. Thus, optimizing the time step is essential to balance accuracy and computational efficiency. Using the optimal mesh from the grid independence study, time steps of 0.33 s, 1 s, 3 s, 9 s, and 27 s are evaluated (Fig. 3b). The results indicate that the time-averaged temperature remains nearly constant for time steps of 3 s and smaller. Specifically, the relative error is approximately 1.07% between 27 s and 9 s, 0.48% between 9 s and 3 s, 0.16% between 3 s and 1 s, and 0.11% between 3 s and 0.33 s. Therefore, a 3 s time step is selected for the subsequent simulations.
- **Comparison with experimental data (validation):** Numerical results are compared with experimental data from cell $T_{2,04}$. The T_{avg} of the top surface is matched with the T_{avg} from two thermocouples placed on the cell. At the WLTC cycle (the first 1800 s) for Case2 and Case3, the RMSE values are 0.3 °C and 0.8 °C, respectively, while the corresponding MAE values are 0.2 °C and 0.7 °C, respectively. These low error metrics indicate strong alignment with experimental data. A detailed temperature behavior of WLTC cases is discussed in Section 3.6.
Furthermore, the second discharge cycle of Case1 (characterized by high-current discharge operation in the absence of active cooling) is used to further evaluate the model's predictive accuracy under thermally demanding conditions. The comparison between simulated and experimental temperatures yields an RMSE of 0.6 °C and an MAE of 0.5 °C, supporting the model's reliability under extreme operating conditions.

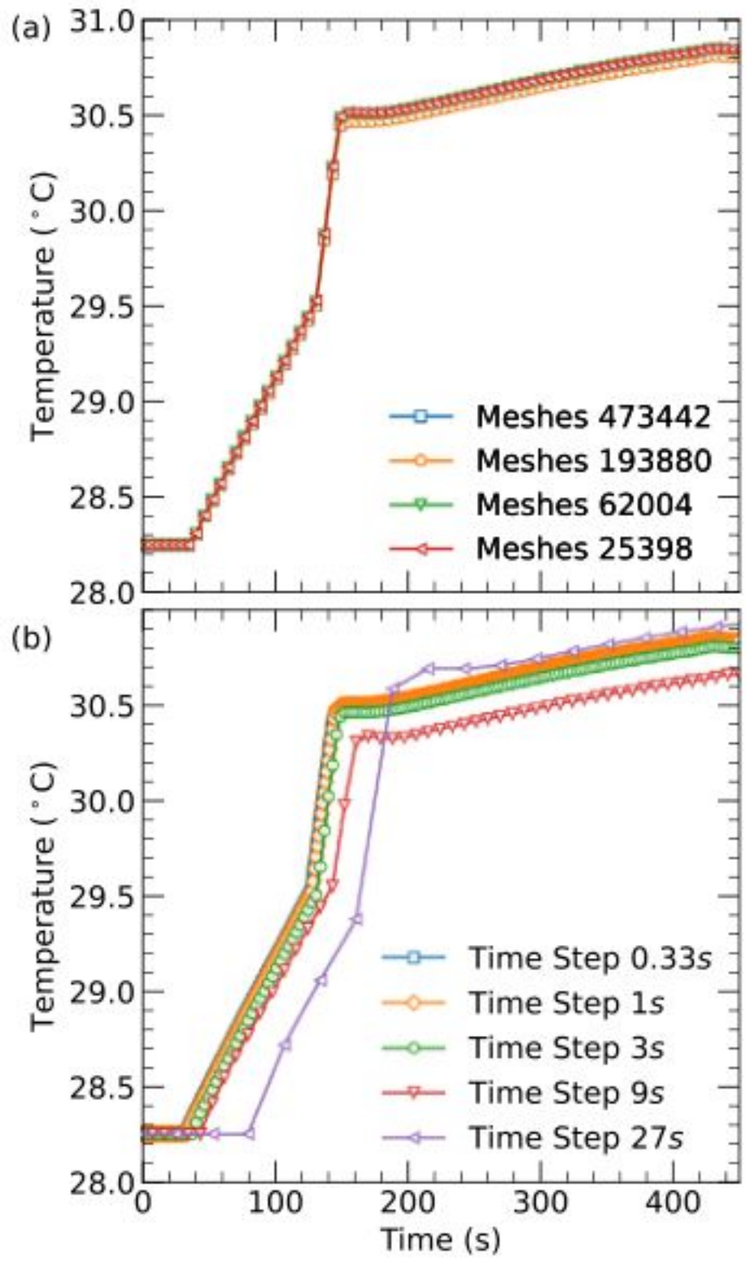

Fig. 3. (a) Mesh independency study with four different mesh sizes; (b) time step independency study with five different time steps.

3.2. Sensitivity analysis of thermophysical parameters

This section presents a sensitivity analysis of ten thermophysical parameters affecting the numerical thermal model of the LIB cell. Each parameter is varied by ±10% from its nominal value, and the resulting effects on model outputs are evaluated. The analyzed parameters include the thermal conductivity, specific heat, and density of the LIB cell, bottom plate, and gap region, as well as the convective heat transfer coefficient to ambient air (see Table 3).

Simulations are conducted using the WLTC current profile (Case2), while keeping all other boundary and initial conditions constant. The influence of each parameter is quantified by calculating the relative error in temperature rise (T_{rise}) during the WLTC phase. This relative error is defined as the percentage difference in T_{rise} between the modified and baseline cases.

The sensitivity results are presented in Fig. 4, where parameters are grouped based on their impact: sensitive and insensitive. Sensitive parameters are those whose variation causes notable changes in T_{rise}, while insensitive parameters show minimal influence on thermal response.

Fig. 4a shows that a 10% decrease in the LIB cell's density and specific heat results in an 8.2% increase in T_{rise}, whereas a 10% increase in these parameters reduces T_{rise} by 6.1% and 6.9%, respectively. A decrease in thermal conductivity causes a minor 0.8% increase in T_{rise}, while its increase results in a 0.1% reduction. As illustrated in Fig. 4b, variations in the convection heat transfer coefficient lead to changes of approximately 0.4% in T_{rise}. Increasing this parameter slightly decreases the T_{rise}, while decreasing it has the opposite effect.

Fig. 4c shows that a ±10% change in the bottom plate's density and specific heat causes an inverse change of approximately ∓0.8% in T_{rise}. Changes in its thermal conductivity, however, have negligible impact. Fig. 4d illustrates that the thermal properties of the gap (thermal conductivity, specific heat, and density) has negligible influence on the model output when altered within ±10%.

In summary, the parameters most sensitive to variation are the specific heat and density of the LIB cell and bottom plate, the LIB cell's thermal conductivity, and the convection heat transfer coefficient of air. Conversely, the thermal conductivity of the bottom plate and all parameters related to the gap region are classified as insensitive due to their limited influence on thermal output.

3.3. State of charge and voltage

In this section, the variations in initial SOC values and their changes over the test period are examined. The SOC represents the amount of energy stored in a LIB cell as a percentage of its total capacity. First, the SOC and voltage profiles for Case1 are examined. Next, Case2 and Case3 are explored, presenting the WLTC and its inverted version. Finally, the remaining two cases, Case4 and Case5, are covered, where additional WLTC profiles are analyzed. It is important to note that in all cases, the cell voltage is assumed as one-twelfth of the pack voltage.

3.3.1. Fully charging and discharging - Case1

Fig. 5 provides a comprehensive visualization of the voltage, current, and SOC for Case1. In this figure, and the subsequent figures in this section, the LIB pack current, voltage, and SOC are represented by the abbreviations I_{pack}, V_{pack}, and SOC_{pack}, respectively. The applied current varies from a minimum value of −237 A to a maximum value of 237 A. For a more thorough analysis, the test duration of Case1 has been divided into two sections for each of the five cycles, namely the discharge period (D) and the charge period (C). Numerical identifiers from 1 to 5 have been assigned to each abbreviation, corresponding to cycles 1 through 5, respectively.

In the initial section of the first cycle (D1) shown in Fig. 5, the current is maintained at −237 A for 140 s, leading to a variation of the SOC from 47% to 10%. During this period, both the pack voltage and cell voltage decrease from 44.16 V and 3.68 V to 39.24 V and 3.27 V, respectively. In the second section of the first cycle (C1), the current is kept constant at 237 A until 226.5 s, which results in an SOC of 33% and an increase in pack voltage to 44.71 V (high current charging segment). Following this, the current decreases to 33 A, leading to an SOC of 91% and a rise in pack voltage to 48.68 V.

The second cycle in Fig. 5 starts at 959.5 s (D2). Throughout the subsequent cycles (D2 and C2 to D5 and C5), the pack SOC, current, and voltage exhibit temporal evolution similar to that observed in D1 and C1. The key distinction lies in the discharge periods, as they initiate at the maximum SOC value, unlike the first cycle. The test of Case1 finishes at 5180 s.

3.3.2. WLTC & inverted version - Case2 & Case3

To facilitate a detailed analysis of the results for Case2 to Case5, the WLTC cycle is divided into four phases: low (L), medium (M), high (H), and extra high (ExH) speed segments. The numerical identifiers 1 or 2 associated with each abbreviation indicate the specific WLTC cycle or its inverted version, respectively. Therefore, Case2 and Case3 include the numbers 1 and 2, as they encompass the WLTC cycle and its inverted version. In Case4 and Case5, only the number 1 is present, as they exclusively involve the WLTC cycle.

Fig. 6 illustrates the voltage, current, and SOC of the battery pack for Case2. The SOC values recorded at the end of the WLTC segments L1, M1, H1, and ExH1 are 91%, 84%, 82%, and 73%, respectively. This trend reflects a 1% increase in SOC during the initial segment, while subsequent sections exhibit a progressive decrease in stored energy, with the most reduction of 9% observed in ExH1. In contrast, during the inverted WLTC cycle, the SOC values at the end of ExH2, H2, M2, and L2 are 60%, 65%, 66%, and 74%, respectively. Consequently, the stored energy of the battery pack shows a 13% reduction by the end of ExH2, whereas increases were noted in the other segments (refer to Fig. A.21 in Appendix A).

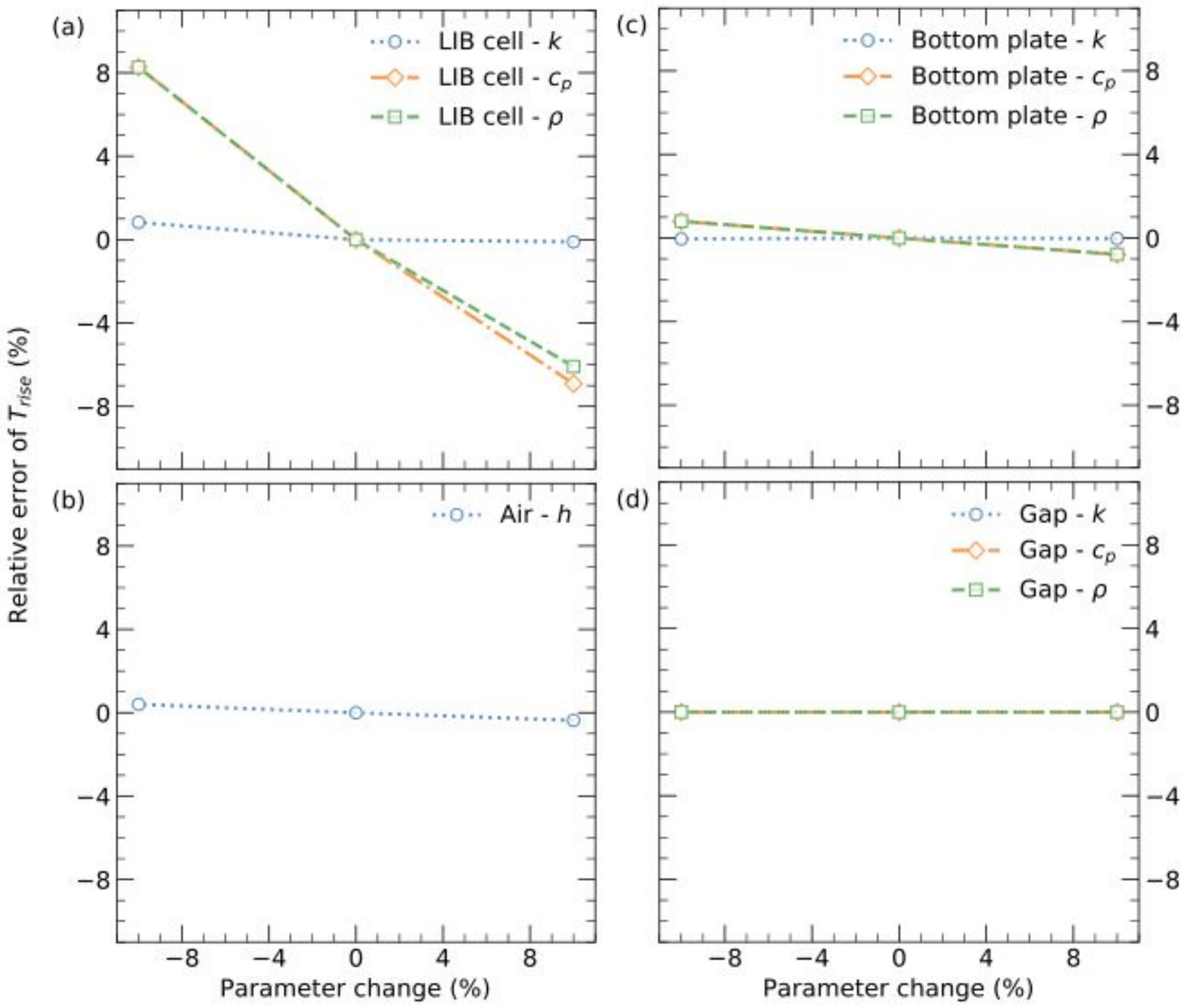

Fig. 4. Sensitivity analysis results showing the impact of thermophysical parameters on temperature rise. (a) LIB cell parameters; (b) air convection coefficient; (c) bottom plate parameters; and (d) gap region parameters (Symbols: k [$\mathrm{W\,m^{-1}\,K^{-1}}$] thermal conductivity, c_p [$\mathrm{J\ kg^{-1}\,K^{-1}}$] specific heat, ρ [$\mathrm{kg\,m^{-3}}$] density, and h [$\mathrm{W\,m^{-2}\,K^{-1}}$] convection heat transfer coefficient).

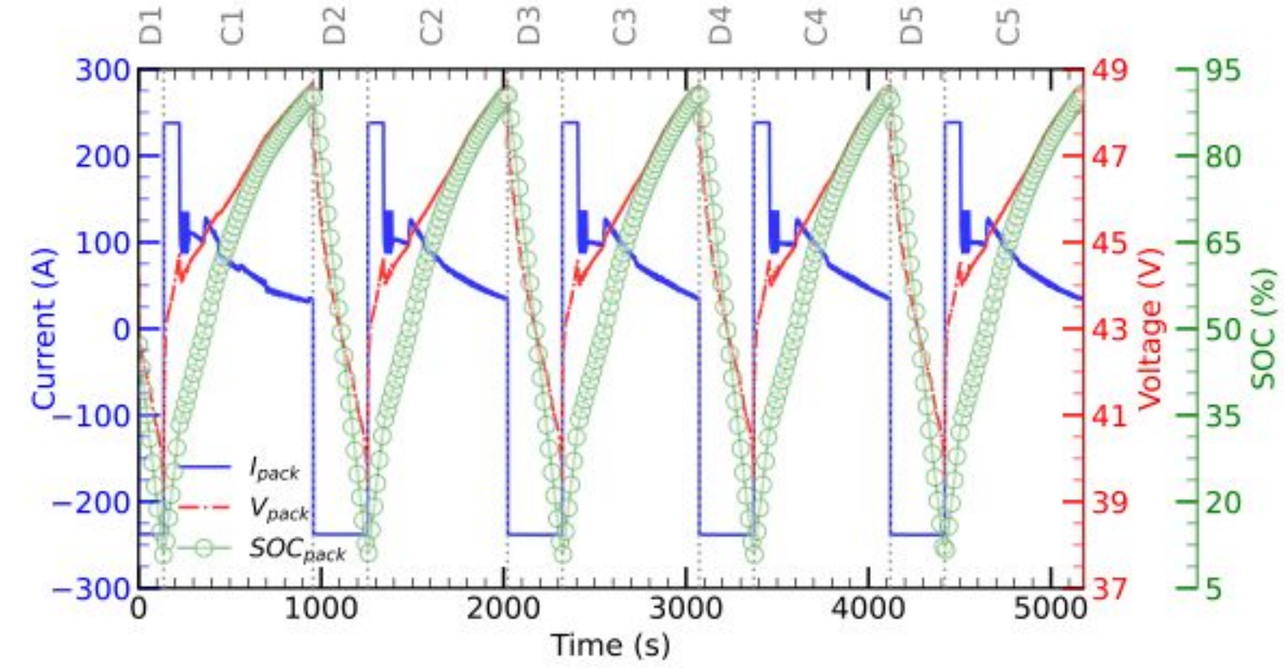

Fig. 5. Current, SOC, and voltage of LIB pack for Case1 (D and C portions represent discharging and charging periods, respectively).

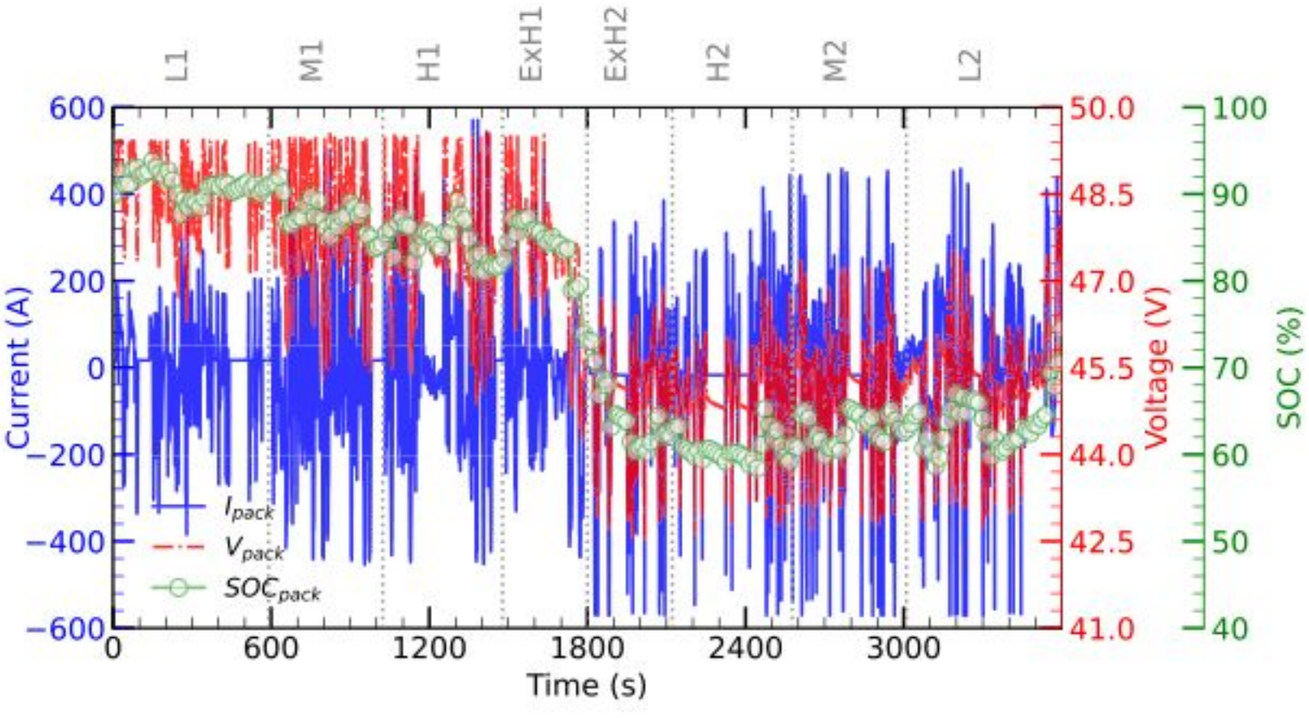

Fig. 6. Current, SOC, and voltage of LIB pack for Case2 (L, M, H, and ExH represent low, medium, high, and extra-high speed sections).

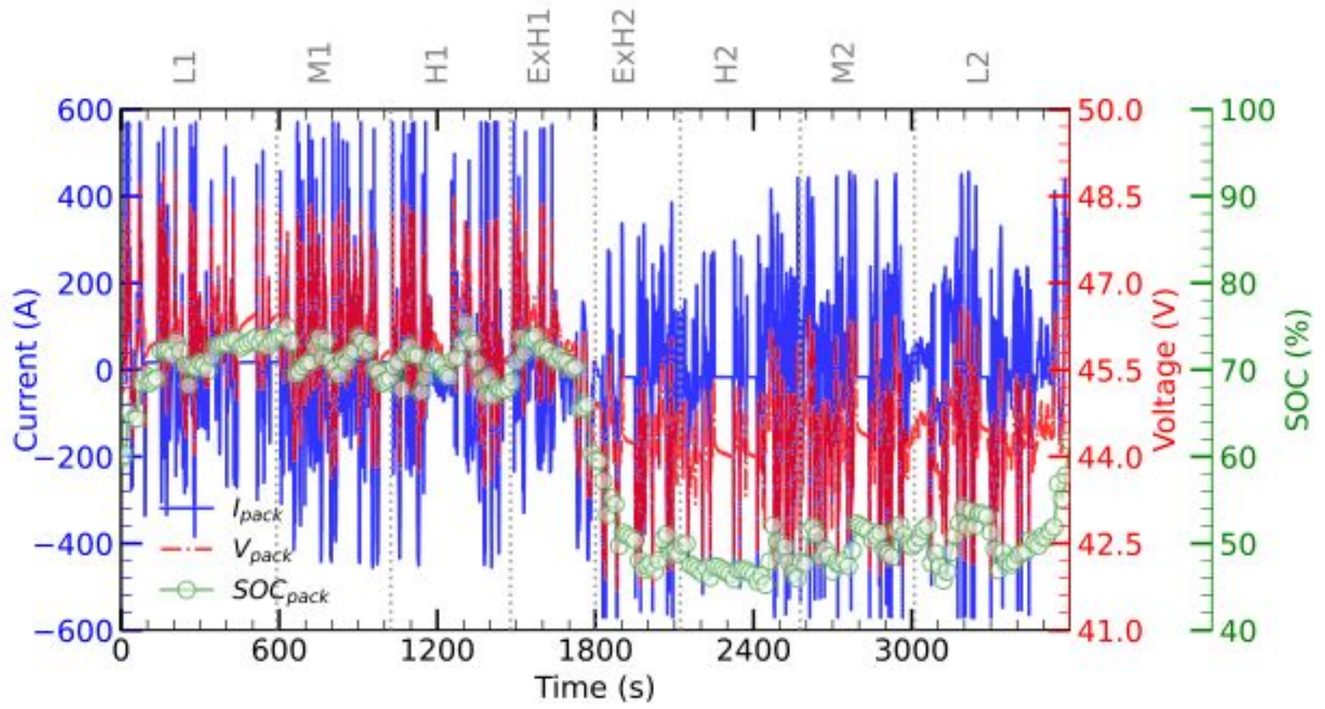

Fig. 7. Current, SOC, and voltage of LIB pack for Case3 (L, M, H, and ExH represent low, medium, high, and extra-high speed sections).

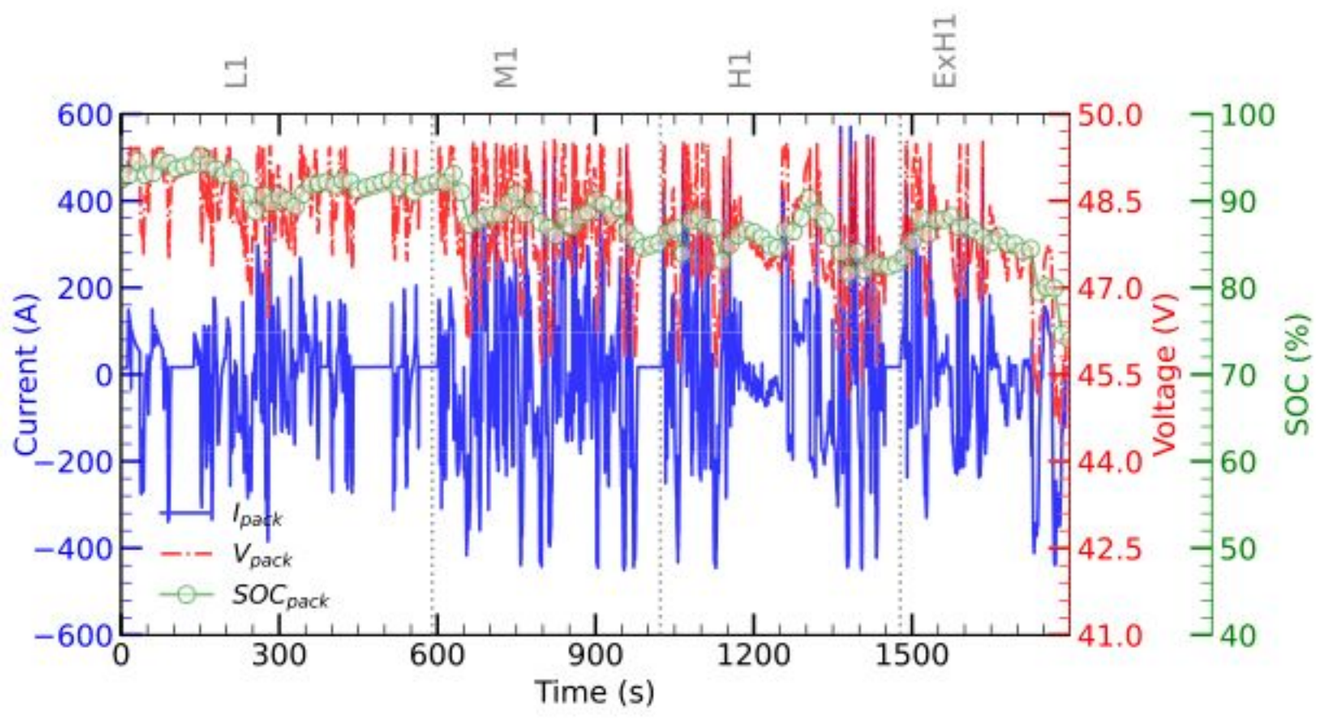

Fig. 8. Current, SOC, and voltage of LIB pack for Case4 (L1, M1, H1, and ExH1 represent low, medium, high, and extra-high speed sections).

Fig. 7 shows the current, voltage, and SOC of the battery pack for Case3, where the test starts with a lower SOC value of 60% compared to Case2. At the end of each section (L1, M1, H1, ExH1, ExH2, H2, M2, and L2), the SOC values are as follows: 74%, 69%, 68%, 60%, 47%, 52%, 53%, and 62%, respectively. Compared to Case2, Case3 demonstrates a greater energy gain during the initial portion (L1), with a 14% increase. However, the stored energy decreases during the subsequent segments of the WLTC, albeit with smaller reductions compared to Case2. The general trend of Case3 aligns with that of Case2; however, the inverted WLTC cycle exhibits lower values overall (refer to Fig. A.21 in Appendix A).

It is worth noting that the SOC decreases by 15% in Case2, while it increases by 2% in Case3 in the complete test period. In Case2, the battery pack reaches a maximum voltage of 49.6 V and a minimum voltage of 42.5 V. In comparison, Case3 exhibits a maximum voltage of 48.8 V and a minimum voltage of 41.7 V.

3.3.3. WLTC - Case4 & Case5

In Case4 and Case5, the driving cycles only include the WLTC. Fig. 8 illustrates the voltage, current, and SOC of the battery pack for Case4. In this case, the initial SOC is 92.5%. At the end of each time portion, the SOC values are as following: 86.96%, 84.74%, 82.89%, and 73% at the end of L1, M1, H1, and ExH1, respectively. It indicates a decrease in SOC in all portions except during M1 portion, where the SOC increased by 0.78% (Fig. A.21 in Appendix A).

Fig. 9 shows the voltage, SOC, and current of the battery pack for Case5. In this case, the initial SOC is approximately 90.5%. At the end of each portion, the SOC values are as follows: 91.86% at the end of L1, 85.25% at the end of M1, 82.94% at the end of H1, and 82.94% at the end of the test (ExH1) (Fig. A.21 in Appendix A). Similar to Case2 and Case3, the SOC decreases in all WLTC portions, except during L1, where the SOC increased by 1.36%.

The minimum pack voltage values for Case4 and Case5 are 44.66 V and 44.70 V, respectively. The maximum voltage recorded for both cases is 49.61 V.

3.4. Thermal behavior of fully charging and discharging - Case1

As mentioned previously, the first portion of all cases is named as passive cooling, indicated by a white background in figures such as Fig. 10. The second section of Case1, Case2, and Case3, involving the liquid cooling system, is termed active cooling and is depicted by the blue background (for example, in Fig. 10). In the figures of this and the following sections, the LIB pack maximum, minimum, and average temperatures are represented by the abbreviations T_{max}, T_{min}, and $T_{avg,Pack}$ (referred to as T_{avg} in the text), respectively. Additionally, the time histories of the average temperatures of Module1, Module2, and Module3 are illustrated using the labels $T_{avg,Module1}$, $T_{avg,Module2}$, and $T_{avg,Module3}$, respectively.

3.4.1. LIB cell thermal behavior - Case1

The temperature time histories of the 25 thermocouples positioned in Module1, Module2, and Module3 are shown in Fig. 10. During the passive cooling phase, $T^{+}_{1,12}$ and $T^{-}_{2,12}$ represent the $T_{min}(t)$ for Module1 and Module2, respectively. $T^{+}_{3,12}$ corresponds to the second-lowest temperature in Module3. However, in the third and fourth cycles, these values increase relative to other points within the same module, and

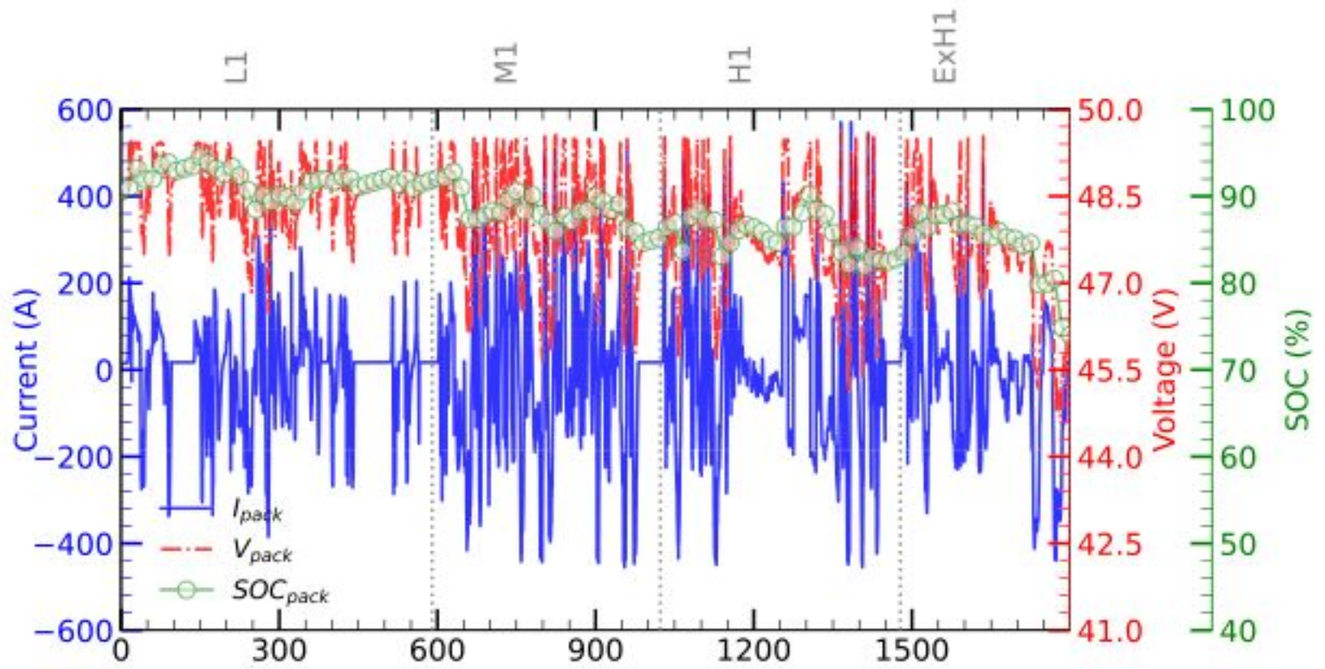

Fig. 9. Current, SOC, and voltage of LIB pack for Case5 (L1, M1, H1, and ExH1 represent low, medium, high, and extra-high speed sections).

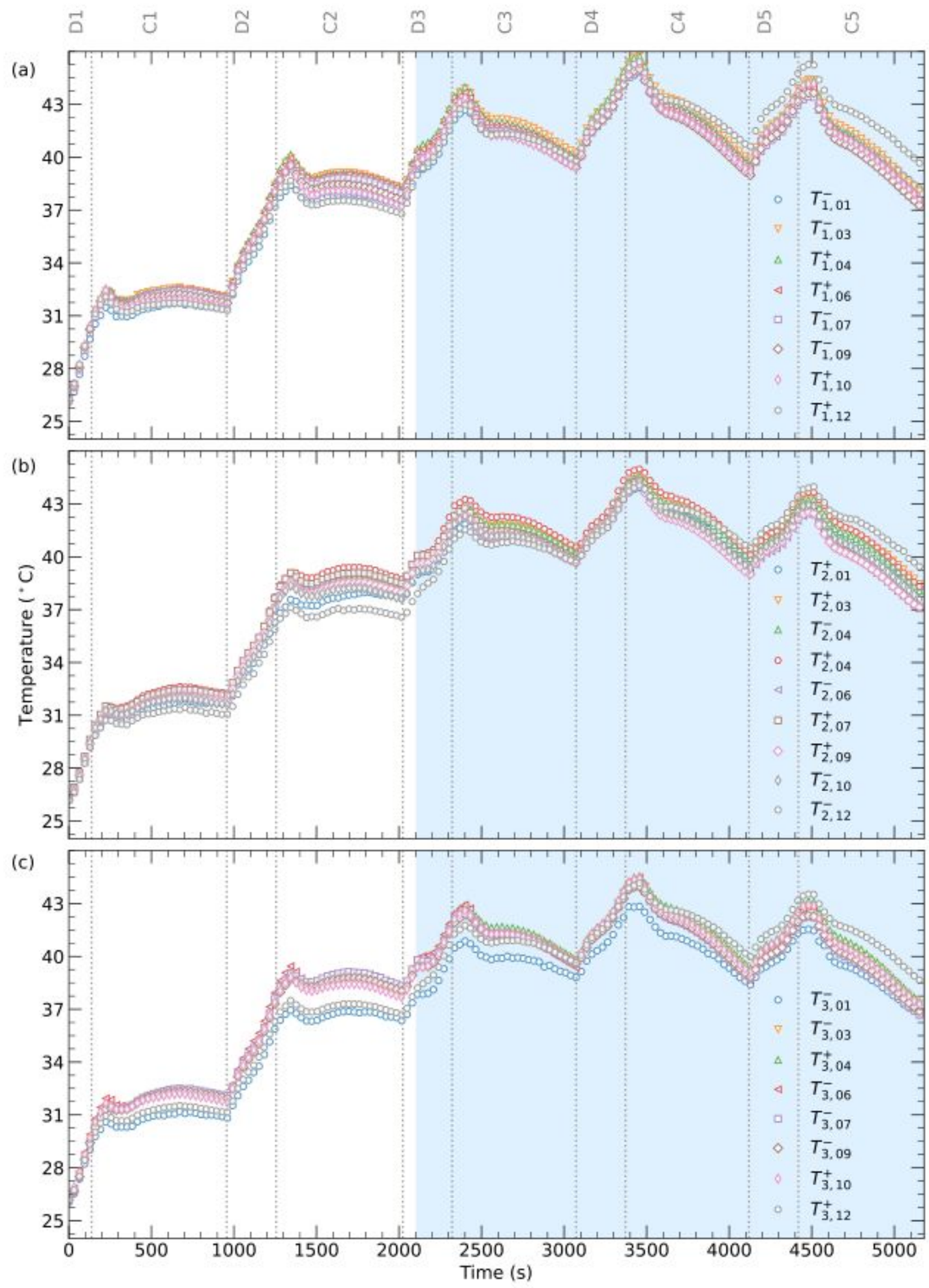

Fig. 10. Temperature time histories of the thermocouples for Case1 placed in (a) Module1, (b) Module2, and (c) Module3. In all plots, the light blue region represents the active cooling phase of the test (D and C portions represent discharging and charging periods, respectively).

by the fifth cycle, they become the $T_{max}(t)$ for the respective module in the active cooling portion.

During the passive cooling phase, the $T_{max}(t)$ is observed in the middle cells; in particular, in Module1, $T_{max}(t)$ is recorded in $T^{-}_{1,03}$, $T^{+}_{1,04}$,

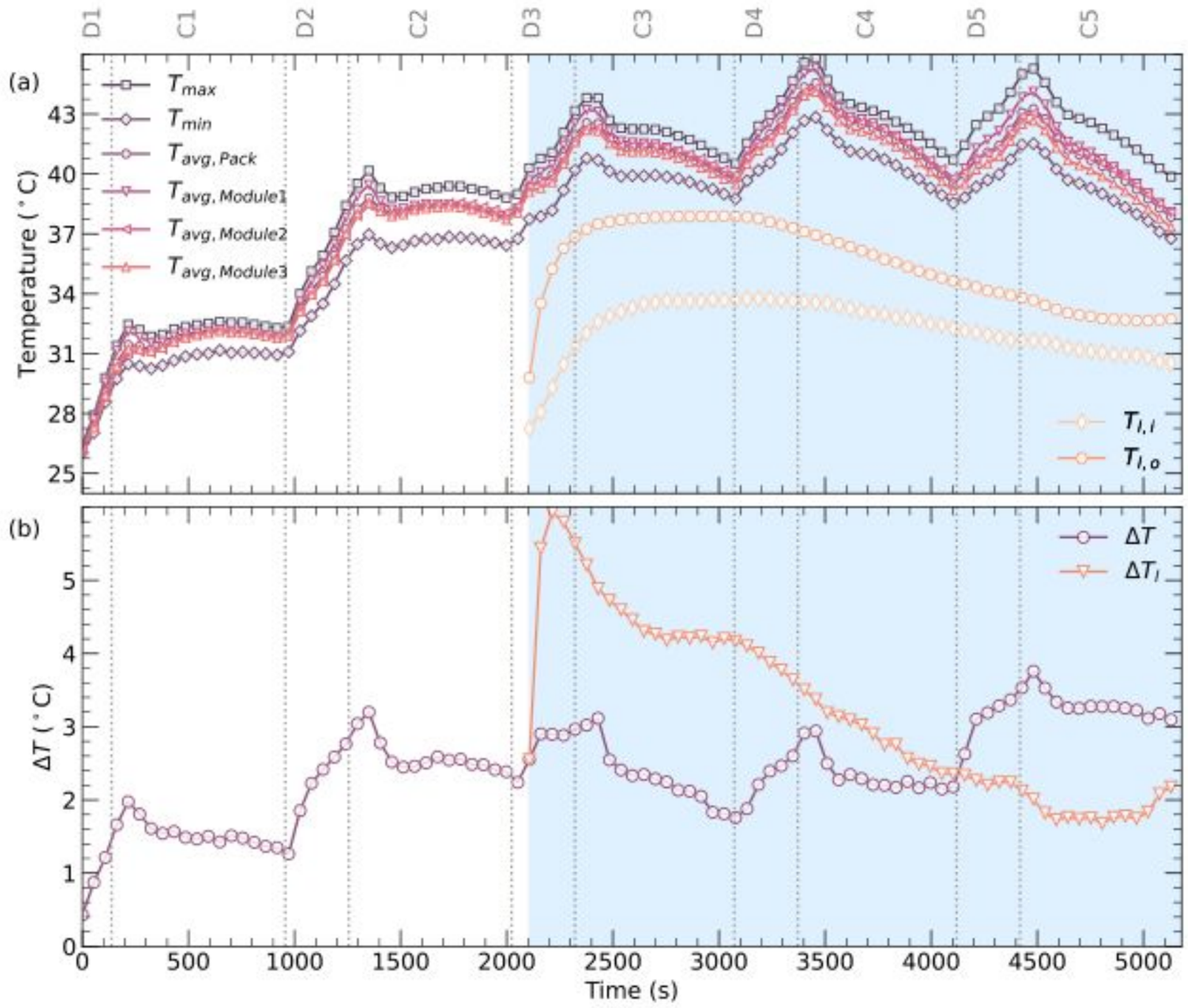

Fig. 11. (a) T_{avg}, T_{max}, and T_{min} of the pack ($T_{avg,Pack}$) and modules ($T_{avg,Module1}$, $T_{avg,Module2}$, and $T_{avg,Module3}$), as well as $T_{l,i}$ and $T_{l,o}$ of the liquid cooling system; (b) ΔT behavior of the LIB pack and ΔT_l of the liquid cooling system in Case1. The active cooling phase is indicated by the light blue shaded region in both plots (D and C portions represent discharging and charging periods, respectively).

and $T^{+}_{1,06}$. In Module2, $T_{max}(t)$ occurs in $T^{+}_{2,04}$ and $T^{+}_{2,07}$. In Module3, $T_{max}(t)$ occurs in three internal cells: $T^{+}_{3,04}$, $T^{-}_{3,06}$, and $T^{-}_{3,07}$. However, in the subsequent cycles, during the active cooling phase, the highest temperatures shift towards the middle or lowest temperature points within each module.

In addition, $T_{min}(t)$ of Module3 consistently occurs in $T^{-}_{3,01}$ throughout all cycles (Fig. 10c). This observation highlights the complexity of the dynamic system and emphasizes the importance of assessing the temperature behavior of a large number of battery cells within a pack during the research phase.

Finally, the temperature time histories of thermocouples positioned near to the negative and positive tabs on the same LIB cell are recorded by $T^{-}_{2,04}$ and $T^{+}_{2,04}$, respectively. The temperature at the positive tab ($T^{+}_{2,04}$) is higher than that at the negative tab ($T^{-}_{2,04}$).

3.4.2. LIB module thermal behavior - Case1

Fig. 10a shows the temperature trends of Module1 throughout each cycle. The $T_{max}(t)$ of Module1 is observed during the charging periods (C1 to C5). In cycles C2 to C5, the maximum temperatures happen at the beginning of the corresponding charging periods, reaching values of 40.2 °C, 44.1 °C, 45.8 °C, and 45.3 °C. These points correspond to the times when the high current charging of 237 A is completed. In contrast to the other charging periods, two peak temperature points are observed in C1, both around 32.7 °C, with the second peak occurring in the middle of the section.

The evolution of the maximum temperature in Module2 and Module3 across the five cycles follows a similar pattern to Module1 from C1 to C5 (Figs. 10b and 10c). The highest temperature values observed for Module1, Module2, and Module3 throughout the entire test occur at the beginning of C4, measuring 45.8 °C, 45.0 °C, and 44.6 °C, respectively.

Fig. 11 presents the time histories of T_{max}, T_{min}, T_{avg}, and ΔT for each module and the entire battery pack. The T_{avg} of Module2 and Module3 follow a trend similar to that of the LIB pack. However, the T_{avg} of Module1 is slightly higher than the pack's average during discharge periods and at the beginning of charging periods, particularly when high currents of 237 A are involved in either charging or discharging. This observation indicates that Module1 is more sensitive to high currents and consequently generates more heat compared to the other modules.

Furthermore, as the test progresses and enters the active cooling phase, the maximum temperature difference between T_{avg} of Module1 and the pack increases with each cycle (Fig. 11a). Specifically, this difference at the end of each high charging period in the passive cooling phase is around 0.6 °C. This difference increases, peaking at 0.9 °C in the final cycle (C5) during the active cooling phase.

3.4.3. LIB pack thermal behavior - Case1

As depicted in Fig. 11a, the maximum T_{avg} of the battery pack occurs during the charging periods (C1 to C5). Notably, these maximum temperatures are observed at the beginning of the respective charging cycles, corresponding to the position between the maximum charging current (237 A) and the remaining time.

During the low current charging periods within the passive cooling portion, the pack's temperature remains relatively stable (Fig. 11a). In contrast, during the active cooling portion, the temperature decreases, leading to a negative T_{rise}. The maximum decrease is observed in C5, where the temperature drops by 5.4 °C from the initial value of 42.9 °C (Fig. 11).

From Fig. 11a, the T_{rise} during a full discharge in the passive cooling portion (D2) is approximately 5.8 °C, starting from an initial T_{avg} of the pack at 31.8 °C. In the active cooling portion, the T_{rise} decreases to 4.2 °C, 4.3 °C, and 3.5 °C for D3, D4, and D5, respectively, with initial T_{avg} values of 37.8 °C, 39.8 °C, and 39.4 °C.

As shown in Fig. 11b, the maximum ΔT values for each cycle occur during the middle of the charging sections, specifically between the high and low charging currents. The maximum ΔT values for cycles one through five are 2.1 °C, 3.3 °C, 3.3 °C, 3.1 °C, and 3.9 °C, respectively.

3.5. Thermal behavior of WLTC cycles - Cases 2 to 5

This section considers the thermal behavior observed in the remaining four cases (Cases 2 to 5). Case2 and Case3 involve a WLTC and its inverted version, while Case4 and Case5 involve only the WLTC cycle.

3.5.1. WLTC & inverted version - Case2 & Case3

Fig. 12a presents the temperature-time history in Module1 of Case2. The $T_{min}(t)$ occurs in $T^{+}_{1,12}$, followed by $T^{-}_{1,01}$ as the second lowest. The $T_{max}(t)$ occurs at $T^{+}_{1,04}$, $T^{-}_{1,03}$, and $T^{+}_{1,06}$. Most temperatures follow a consistent pattern throughout the driving cycle, except during a brief abnormality from 350 s to 800 s (from the middle of L1 to the middle of M1), where $T^{+}_{1,06}$ deviates (illustrated in a zooming box on the left top of Fig. 12a). This irregularity can be categorized into three phases: initially, a temperature rise of 0.5 °C compared to the second-highest temperature in Module1 at the same moment; next, a temperature disparity of 2.5 °C; and finally, a difference of 0.7 °C using the same comparison criteria. The anomaly disappears within a short duration and does not influence the overall results. Further details are provided in Section 4.2. To ensure precision, data from this temperature point were excluded from the calculations of $T_{max}(t)$, $T_{min}(t)$, $\Delta T(t)$, $T_{avg}(t)$, and T_{rise}.

Fig. 12b illustrates temperature profiles of the points in Module2 of Case2. $T_{max}(t)$ is observed at $T^{+}_{2,04}$, with $T^{+}_{2,07}$ as the second highest, except from the middle of M2 to the end of L2. Initially, $T^{+}_{2,01}$ shows the highest temperature in L1, however, it decreases during M1 and remains the second lowest until the end of the test. $T_{min}(t)$ is found at $T^{-}_{2,12}$.

Fig. 12c illustrates the temperature behavior of various cells in Module3 of Case2. $T_{min}(t)$ occurs in $T^{-}_{3,01}$, followed by $T^{+}_{3,12}$. On the other hand, the $T_{max}(t)$ is observed in $T^{+}_{3,04}$ and $T^{-}_{3,06}$. Except for $T^{-}_{3,01}$ and $T^{+}_{3,12}$, all other temperature points are in close alignment with the maximum temperature range.

The $T_{avg}(t)$ profiles of Module2 and Module3 in Case2 exhibit a trend similar to Module1 during L1, with slightly lower values for the remaining periods (Fig. B.22 in Appendix B). By the end of the WLTC, the $T_{avg}(t)$ values for Module1, Module2, and Module3 in Case2 are 34.8 °C, 34.1 °C, and 34.0 °C, respectively. By the end of the inverted WLTC, these values increase to 39.5 °C, 38.7 °C, and 38.3 °C, respectively. In all modules, the highest $T_{avg}(t)$ occurs at the beginning of M2 (around 2960 s) when the liquid cooling system is activated, and again in the middle of L2 (around 3260 s).

Fig. 13a shows temperature profiles for Module1 in Case3. $T_{max}(t)$ occurs at $T^{+}_{1,04}$ and $T^{+}_{1,06}$, with $T^{+}_{1,06}$ generally having a higher temperature. $T_{min}(t)$ fluctuates between $T^{-}_{1,01}$ and $T^{+}_{1,12}$.

Fig. 13b illustrates temperature variations in Module2 of Case3. Throughout all time sections, $T^{+}_{2,04}$ consistently records the $T_{max}(t)$. Furthermore, $T^{+}_{2,07}$ exhibits a high temperature during the test, except from the middle of M2 to the end of L2. Conversely, the $T_{min}(t)$ of Module2 is observed at $T^{-}_{2,12}$. As in Case2, $T^{+}_{2,01}$ in Case3 initially exhibits the $T_{max}(t)$ during the L1 section; however, its rate of T_{rise} decreases and remains the second lowest in the module from the middle of M1 (around 650 s) until the end of the test.

Fig. 13c presents the temperature profiles of various points in Module3 for Case3. Initially, $T^{-}_{3,01}$ starts within the mid-range of temperatures during the first 100 s, but its T_{rise} rate slows down, making it the lowest temperature point in Module3 from the middle of L1 onward. $T^{+}_{3,12}$ consistently shows the second lowest temperature. Conversely, $T_{max}(t)$ is observed at $T^{+}_{3,04}$, while the second highest temperature alternates among $T^{-}_{3,06}$, $T^{-}_{3,09}$, and $T^{+}_{3,10}$, all of which are internal temperature points.

The $T_{avg}(t)$ profiles for Modules 1, 2, and 3 in Case3 are similar, with values at the end of the WLTC at 35.4 °C, 35.0 °C, and 34.9 °C, respectively, and at the end of the inverted WLTC at 39.5 °C, 39.0 °C, and 38.7 °C, respectively (Fig. B.22 in Appendix B). As in Case2, the highest $T_{avg}(t)$ occurs at the beginning of M2 (at 2900 s when the liquid cooling system is activated) and in the middle of L2 (around 3260 s).

Fig. 14 illustrates the time-averaged $T_{avg}(t)$ for each time section in Case2 and Case3, along with the corresponding time-averaged $\Delta T(t)$ at the specified time sections. In both cases (Case2 and Case3), time-averaged temperature increases gradually throughout the test, peaking during H1 (with increases of 3.2 °C in Case2 and 3.0 °C in Case3) and M2 (with increases of 3.0 °C in Case2 and 3.1 °C in Case3). Conversely, in L2, where the cooling system is active, the time-averaged temperature decreases. Despite Case3 showing slightly higher temperatures than Case2, both follow a similar trend.

In Case2, the pack $T_{avg}(t)$ increases by 10.5 °C and 4.6 °C in the first WLTC and inverted WLTC periods, respectively. Similarly, in Case3, the $T_{avg}(t)$ rises by 11.4 °C and 4.0 °C in the first WLTC cycle and inverted WLTC cycle, respectively (Fig. B.22 in Appendix B).

Additionally, the time-averaged $\Delta T(t)$ for Case2 is 0.7 °C in L1 and increases throughout the test, except during L2. Case3 exhibits a similar pattern but with higher values in L1 (1.2 °C) and M1, almost the same value in H1, and lower values in the remaining time sections. The

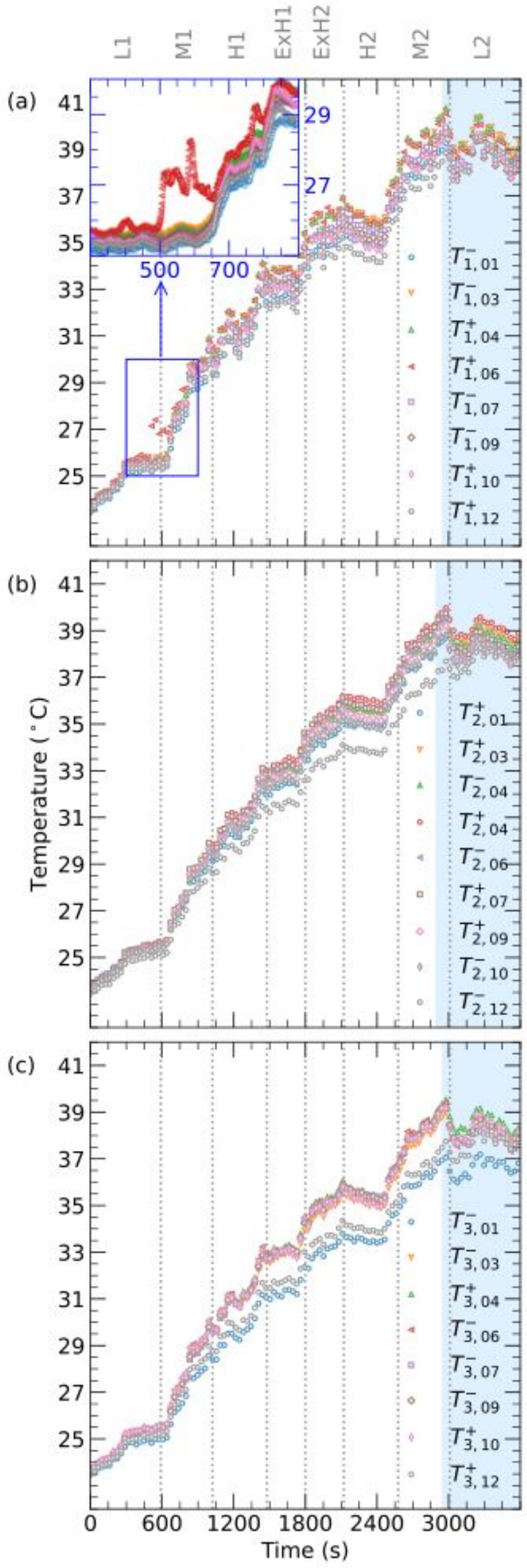

Fig. 12. Temperature time histories in Case2 of the thermocouples placed in (a) Module1, (b) Module2, and (c) Module3. The active liquid cooling period is highlighted in blue (L, M, H, and ExH represent low, medium, high, and extra-high speed sections).

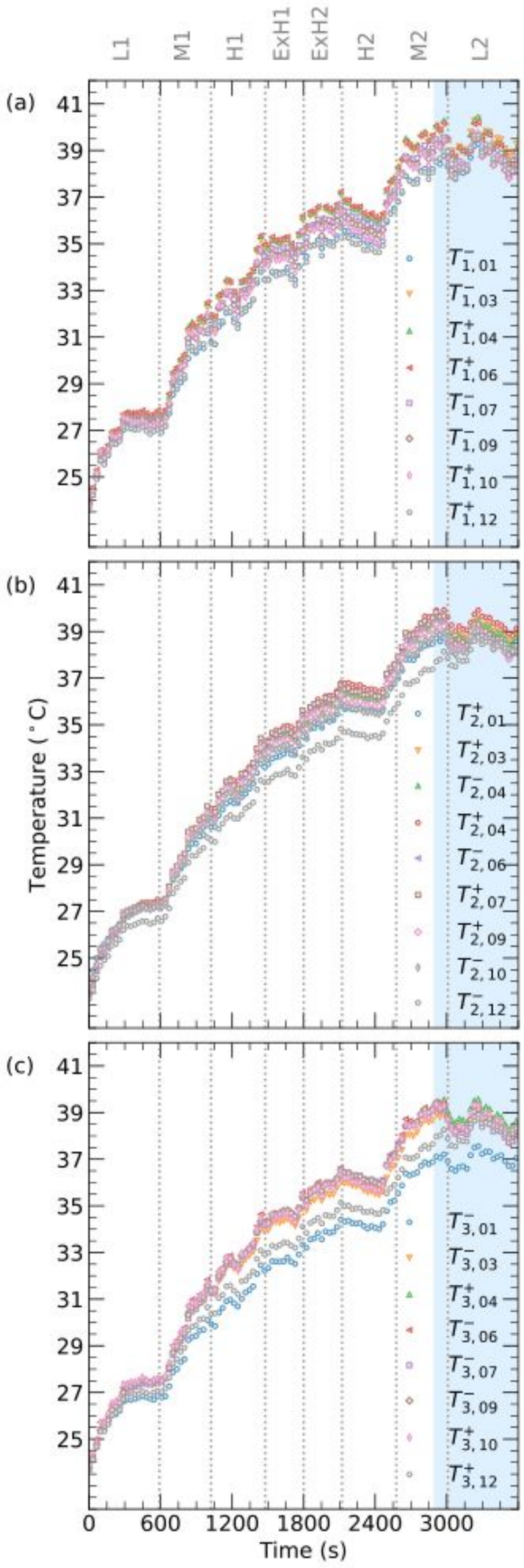

Fig. 13. Temperature time histories in Case3 of the thermocouples placed in (a) Module1, (b) Module2, and (c) Module3. The active liquid cooling period is indicated in blue (L, M, H, and ExH represent low, medium, high, and extra-high speed sections).

maximum time-averaged $\Delta T(t)$ occurs in M2 for both cases, with values of 3.2 °C in Case2 and 2.7 °C in Case3.

3.5.2. WLTC - Case4 & Case5

Fig. 15a illustrates the temperature distribution in the first module of Case4. During the L1 portion, the T_{min} for Module1 occurs at $T^+_{1,10}$, which shifts to $T^+_{1,12}$ from M1 until the end of the cycle. The T_{max} in Module1 fluctuates between $T^+_{1,04}$ and $T^-_{1,03}$.

Fig. 15b presents the temperature profiles for Module2 in Case4. Throughout the test, T_{min} consistently occurs at $T^-_{2,12}$. On the other side, initially, $T^+_{2,01}$ is placed as the highest temperature in the L1 phase but shifts to the second lowest temperature from the middle of M1. In this module, the T_{max} fluctuates between $T^+_{2,04}$ and $T^+_{2,07}$.

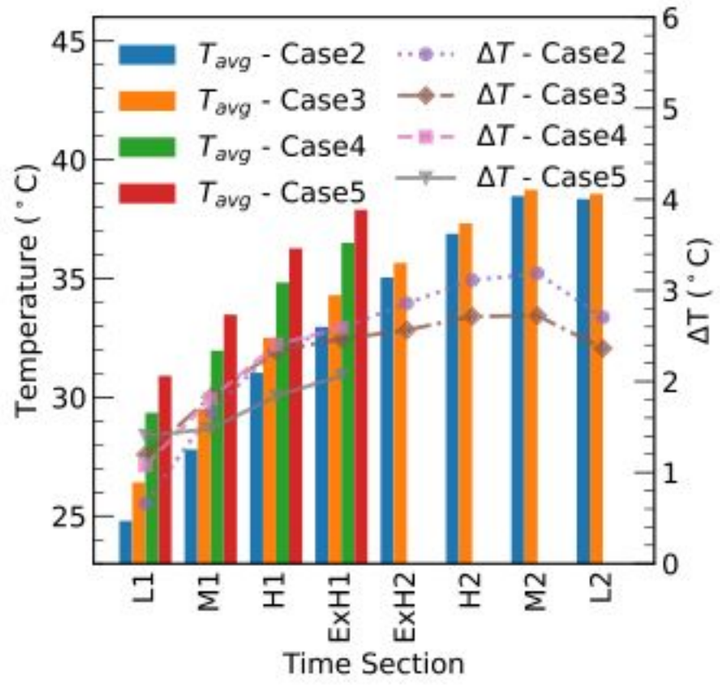

Fig. 14. Time section averages of the $T_{avg}(t)$ for the LIB pack for Case2, Case3, Case4, and Case5 as well as the relative $\Delta T(t)$s. L, M, H, and ExH represent low, medium, high, and extra-high speed sections.

Fig. 15c shows the temperature distribution in Module3 of Case4. The T_{min} is observed at $T^-_{3,01}$, with the second lowest temperature at $T^+_{3,12}$. The highest temperature points in this module are found in the central cells.

At the beginning of the test, T_{avg} for Module1 is intermediate between Module2 and Module3 (28.4 °C, 28.7 °C, and 28.1 °C, respectively). However, by the beginning of M1, the T_{avg} of Module1 shifts to the highest value among the three modules. Fig. B.23 in Appendix B shows the $T_{avg}(t)$ for all three modules and the battery pack. At the end of the test, $T_{avg}(t)$ values are 38.0 °C for Module1, 37.5 °C for Module2, and 37.2 °C for Module3.

Fig. 16a shows the temperature profiles for Module1 in Case5. T_{min} consistently occurs at $T^+_{1,12}$, with the second lowest temperature at $T^-_{1,01}$. The T_{max} alternates between $T^+_{1,04}$ and $T^-_{1,03}$.

Fig. 16b depicts the temperature profiles for Module2 in Case5. T_{min} is consistently at $T^-_{2,12}$. Furthermore, outside the L1 phase, $T^+_{2,01}$ records the second lowest temperature. In L1, the T_{max} occurs in $T^+_{2,07}$ and the second lowest temperature point is $T^+_{2,04}$. Then, the highest temperature fluctuates between the two points (outside of the L1 portion).

Fig. 16c shows the temperature profiles for Module3 in Case5. T_{min} alternates between $T^+_{3,12}$ and $T^-_{3,01}$. The T_{max} is found in the internal cells with no fixed cell consistently having the maximum temperature.

Similar to Case4, in Case5, Module1 initially has the lowest $T_{avg}(t)$ during L1, but shifts to higher values during M1, H1, and ExH1 (shown in Fig. B.23c in Appendix B). The $T_{avg}(t)$ values at the beginning are 29.5 °C, 30.0 °C, and 30.1 °C for Modules 1, 2, and 3, respectively, and at the end of ExH1 are 39.1 °C, 38.9 °C, and 38.8 °C, respectively. Finally, when comparing Case4 and Case5, the $T_{avg}(t)$ differences between modules in Case5 are smaller than in Case4 during M1, H1, and ExH1 portions.

In both Case4 and Case5, the time-averaged temperature gradually increases throughout the test, as shown in Fig. 14. Although Case5 exhibits slightly higher temperatures than Case4, both follow a similar trend, peaking during H1 with an increase of 2.8 °C in both cases.

The $T_{avg}(t)$ for the pack increases by 9.1 °C during the WLTC period for both Case4 and Case5 (Fig. B.23 in Appendix B). The peak $T_{avg}(t)$ for the pack occurs at the end of the cycle, reaching 38.9 °C for Case4 and 37.5 °C for Case5. Therefore, in these two cases, the cooling system remains inactive.

Furthermore, the time-averaged $\Delta T(t)$ for Case4 is 1.1 °C in L1 and increases throughout the test, similar to Cases 2 and 3. In Case5, the initial $\Delta T(t)$ in L1 is 2.0 °C, higher than the other cases. As shown in Fig. 14, the average $\Delta T(t)$ of Case5 remains almost constant during L1 and M1 portions, and is lower than the other cases during the remaining portions of the WLTC cycle.

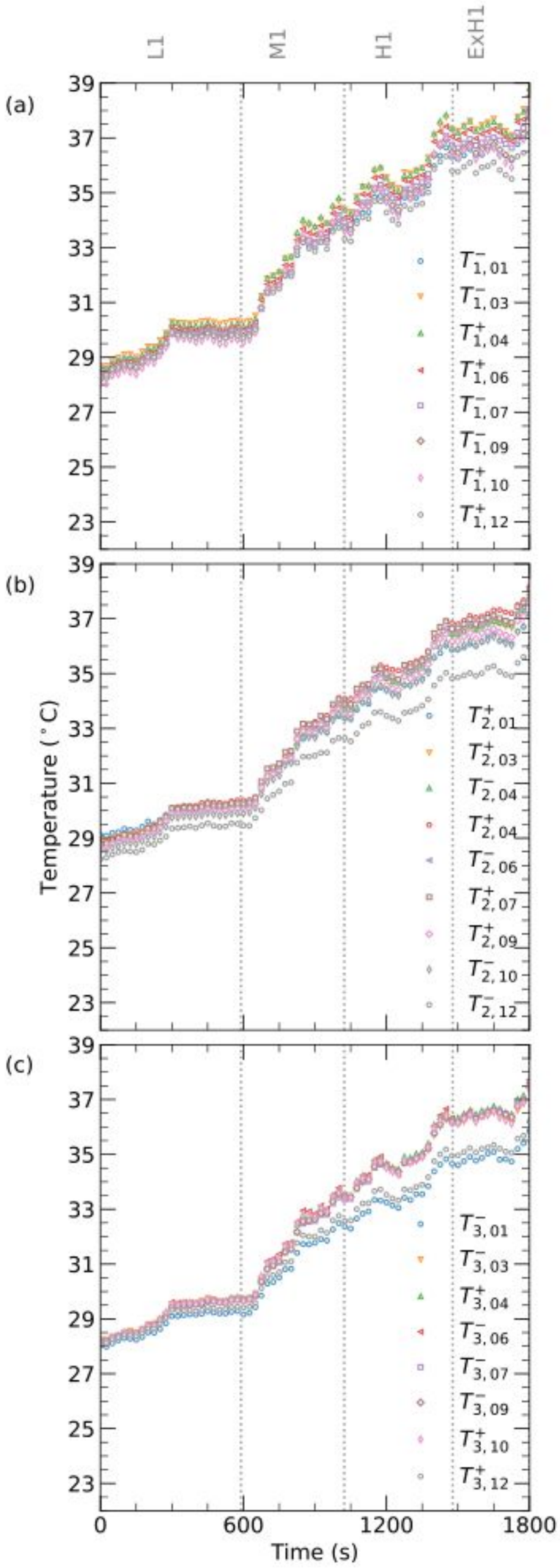

Fig. 15. Temperature time histories in Case4 of the thermocouples placed in (a) Module1, (b) Module2, and (c) Module3 (L1, M1, H1, and ExH1 represent low, medium, high, and extra-high speed sections).

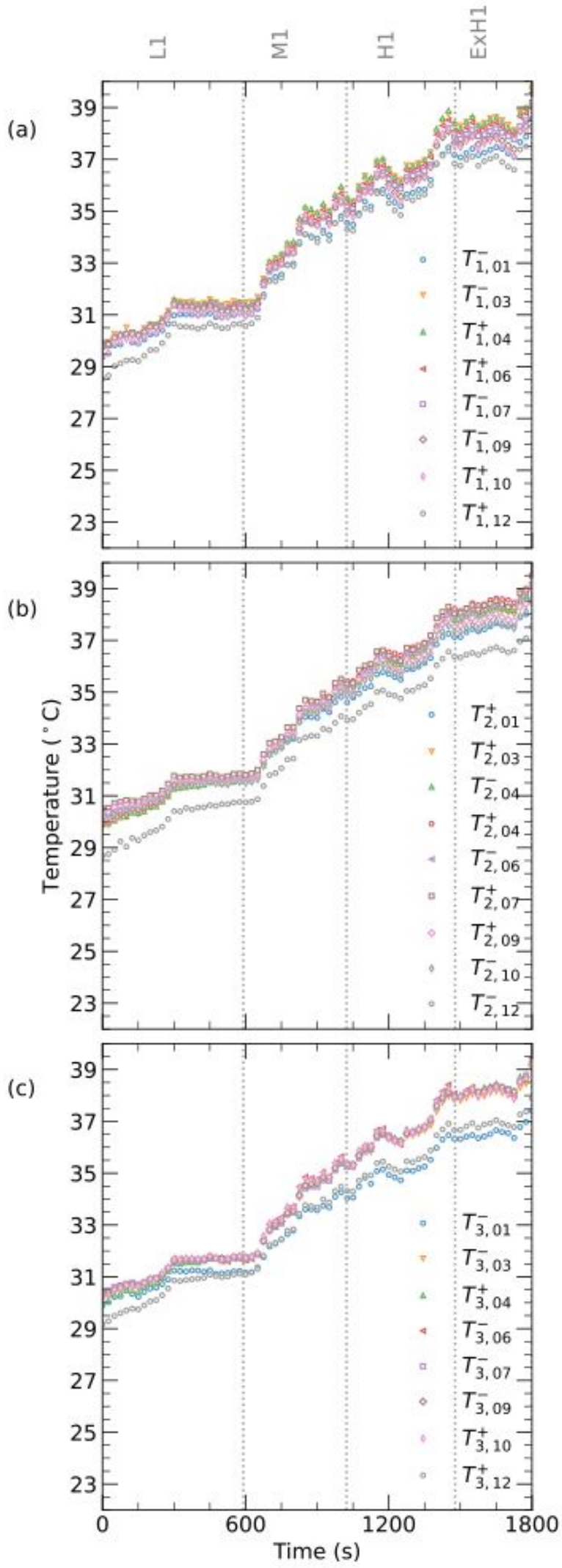

Fig. 16. Temperature time histories in Case5 of the thermocouples placed in (a) Module1, (b) Module2, and (c) Module3 (L1, M1, H1, and ExH1 represent low, medium, high, and extra-high speed sections).

3.6. Indirect liquid cooling system behavior

In this section, the performance of the cooling system in Case1, Case2, and Case3 is investigated. The first subsection reports the experimental results of Case1, where the constant C-rates with and without the cooling system allow for comparative analysis. Subsequently, the results for the cooling system in Case2 and Case3 are presented, including experimental data on the cooling system activation timing and temperature, along with numerical results for evaluating the impact of the cooling system.

3.6.1. Fully charging and discharging - Case1

The temperature rise during all discharge periods (Ds) in Case1 follows a monotonic trend, with the exception of D3 (Fig. 11a). This deviation is likely due to the initial activation of the liquid cooling system, which takes place midway through D3. In Fig. 11, the inlet ($T_{l,i}$) and outlet ($T_{l,o}$) temperatures of the liquid cooling system are depicted, along with their difference, denoted as ΔT_l. During this phase, an initial rise in $\Delta T_l(t)$ is observed, indicating enhanced heat absorption from the battery pack (Fig. 11b). This temporary change in the T_{rise} slope is driven by the rise of $\Delta T_l(t)$. The maximum value of $\Delta T_l(t)$ in Case1 is about 6.0 °C and occurs shortly after the initial time of the active cooling phase (around $100s$). This peak value is maintained for about 60 s before gradually decreasing. The lowest value of $\Delta T_l(t)$, reached during C5, is approximately 1.7 °C.

The active cooling system in Case1 is activated at 2102 s, when the $T_{max}(t)$, T_{avg}, and ΔT of the LIB pack reach 40.2 °C, 39.3 °C, and 2.5 °C,

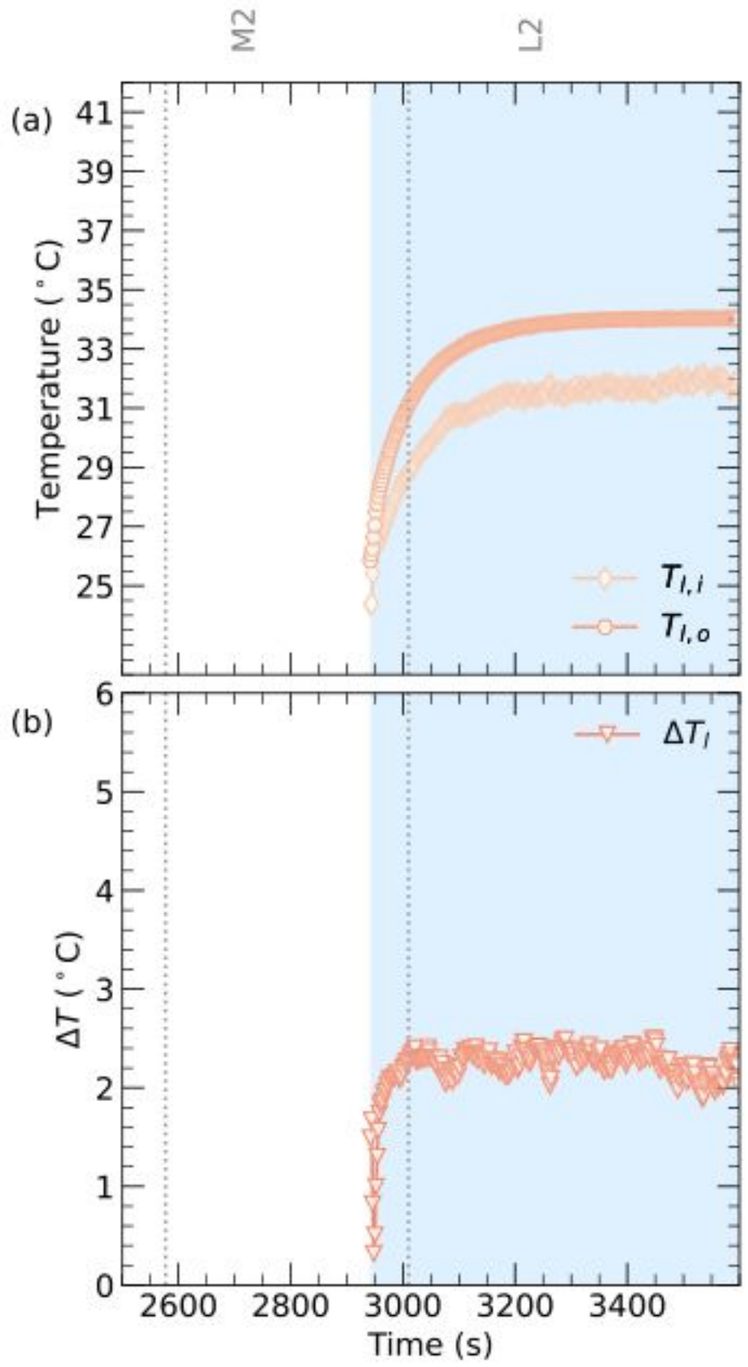

Fig. 17. (a) Inlet ($T_{l,i}$) and outlet ($T_{l,o}$) temperatures of the liquid cooling system, along with (b) their temperature difference (ΔT_l) for Case2 during M2 and L2. M2 and L2 represent medium and low speed sections in the inverted version of the WLTC.

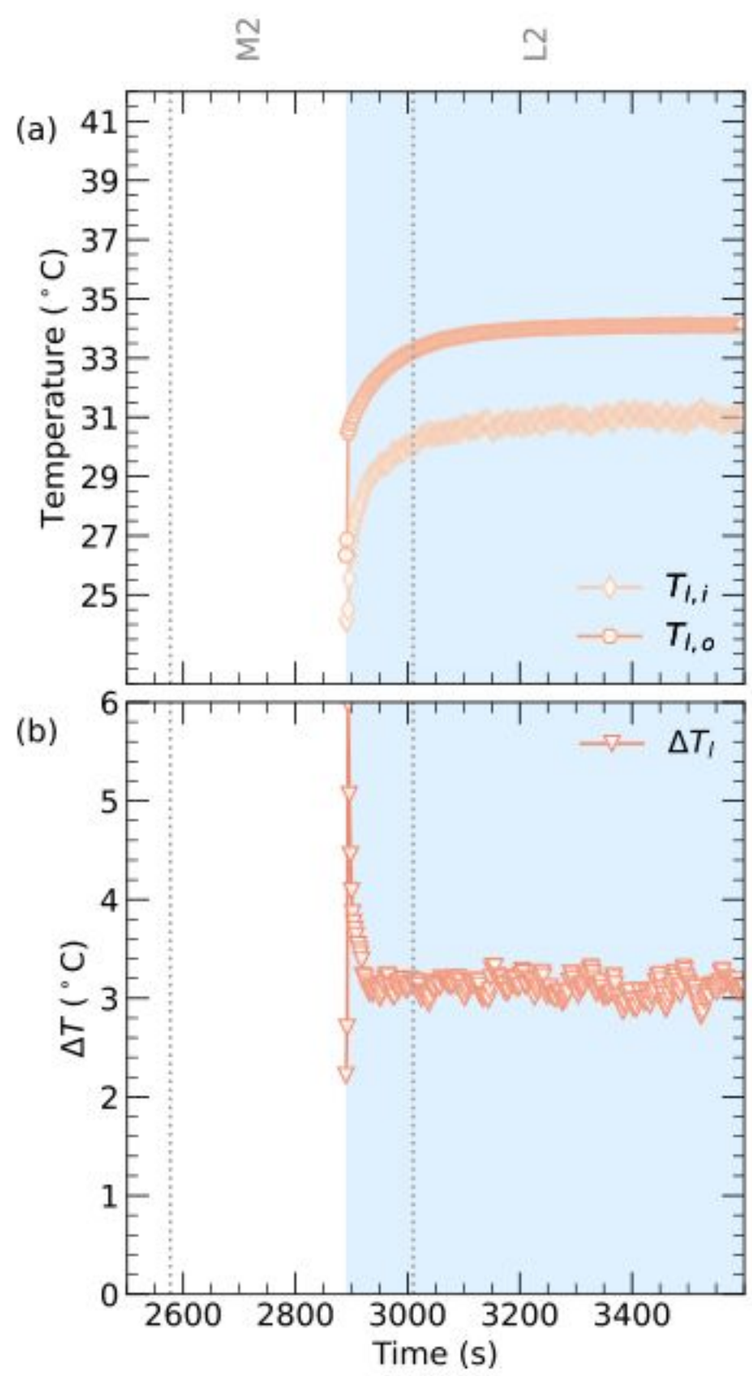

Fig. 18. (a) Inlet ($T_{l,i}$) and outlet ($T_{l,o}$) temperatures of the liquid cooling system, along with (b) their temperature difference (ΔT_l) for Case3 during M2 and L2. M2 and L2 represent medium and low speed sections in the inverted version of the WLTC.

respectively (Fig. 11). $T_{l,i}(t)$ starts at 27.2 °C, peaks at 37.9 °C during the middle of C3, and remains at this maximum until the end of D4. Subsequently, it gradually decreases, reaching 32.7 °C by the end of the test. Similarly, $T_{l,o}(t)$ exhibits the same general trend but remains consistently higher due to heat absorption throughout the test cycles. The behavior of ΔT during the third cycle mirrors the temperature behavior and is impacted by the activation timing of the liquid cooling system (Fig. 11b).

3.6.2. WLTC - Case2 & Case3

Figs. 17a and 18a present the $T_{l,i}(t)$ and $T_{l,o}(t)$ for both Case2 and Case3, respectively. As previously indicated, the liquid cooling system activates approximately midway through the M2 phase, specifically at 2942 s for Case2 and 2890 s for Case3. Therefore, the active liquid cooling system operates during the final 18% and 20% of the test time for Case2 and Case3, respectively. The values of $\Delta T_l(t)$ are approximately 3.1 °C for Case2 and 2.2 °C for Case3 (Figs. 17b and 18b). In Figs. 17 and 18, it can be observed that $T_{l,o}(t)$ and $T_{l,i}(t)$ in L2 for both cases remain almost steady-state, with $T_{l,o}(t)$ for both cases being around 34.0 °C.

To investigate the indirect liquid cooling system performance in Case2 and Case3, the thermal behavior is simulated numerically (as detailed in Section Section 2.6). Fig. 19 illustrates the thermal behavior of $T_{2,04}$ with the activated cooling system (experimental results) and without the activated cooling system (numerical results). The reported temperature is the average temperature of the top surface of the LIB cell. Furthermore, for each case presented in Fig. 19, the temperature distribution across the LIB cell at the end of the test is depicted, with the right legend indicating the corresponding temperature contour values.

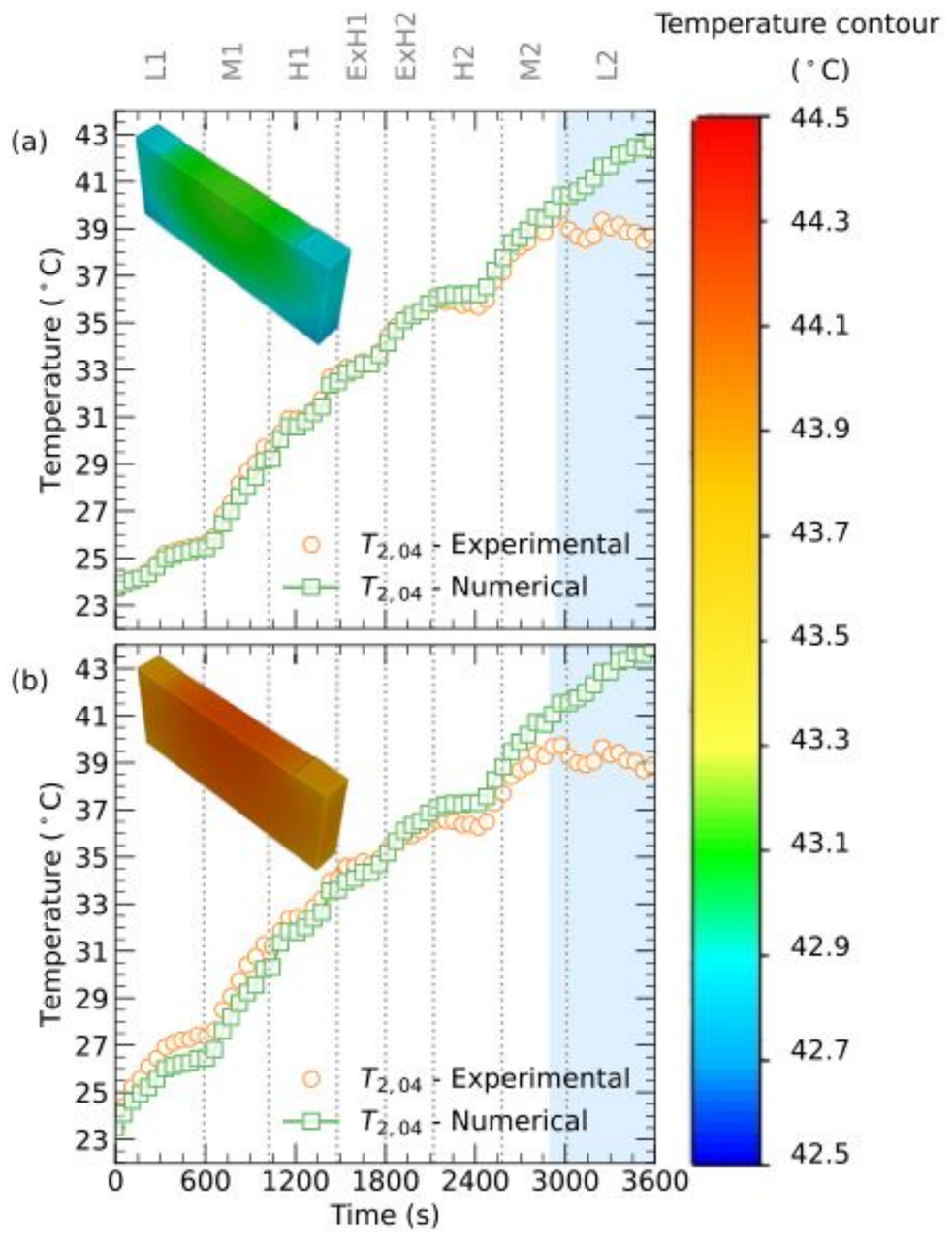

Fig. 19. Experimental and numerical temperature behavior of $T_{2,04}$ for (a) Case2 and (b) Case3. L, M, H, and ExH represent low, medium, high, and extra-high speed sections.

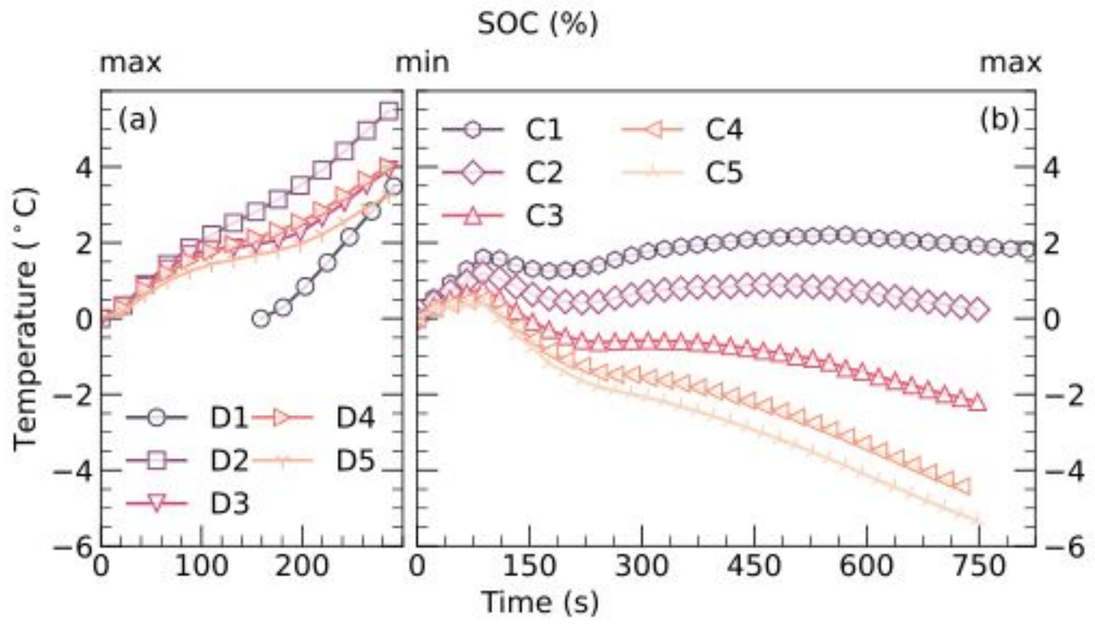

Fig. 20. Average pack temperature time histories for Case1 placed in (a) discharging and (b) charging cycles. D and C portions represent discharging and charging periods, respectively.

Fig. 19a shows that in the last 18% of the test in Case2, the LIB cell temperature reduces from 38.8 °C to 38.6 °C with the activated cooling system (a reduction of 0.2 °C). In contrast, without the activated cooling system, the temperature increases from 39.4 °C to 42.4 °C (a T_{rise} of 3.0 °C).

Fig. 19b indicates that in the last 20% of the test in Case3, the temperature decreases from 39.5 °C to 39.2 °C (a decrease of about 0.3 °C) with the activated cooling system. Without the activated cooling system, the temperature increases by 3.4 °C from an initial temperature of 40.8 °C.

This study focuses on the LIB thermal response without modeling active cooling in the simulation. However, future simulations could incorporate the cooling system's activation to evaluate different control strategies and activation timings. This would require a detailed thermal-fluid model at the module or pack level, and can build upon the validated cell-level data presented in this study.

4. Discussion

This section provides a comprehensive analysis of different aspects of the experimental and numerical results, focusing on the SOC behavior under various dynamic profiles, the detailed thermal performance of the cells, modules, and pack under different dynamic loads, the overall efficiency of the indirect liquid thermal management system for the pack, and the contribution of the sensitivity analysis to evaluating model robustness and identifying critical thermophysical parameters.

4.1. State of charge analysis

The SOC serves as a crucial parameter in battery system analysis, influencing energy availability and overall performance [33,56]. While much of the literature on LIB cell analysis focuses on SOC limitations, real-world applications often demand sustained high currents for extended periods [57,58]. As a result, the BMS restricts output well below the maximum static limit to prioritize safety and minimize damage. This behavior is illustrated in Fig. 5, where a constant current of 237 A leads to a sudden drop during the latter part of each charging cycle, reflecting the implementation of the BTMS strategies aimed at protecting the battery [57].

In Cases 2 to 5, the highest decrease in SOC occurs during the ExH portions, attributed to high power demands during these periods, particularly in hybrid mode. Comparing Cases 2 to 5, it is evident that Case3 (lowest initial SOC) experiences a smaller reduction in stored energy during certain sections, balancing the final SOC relative to its initial level (Fig. A.21 in Appendix A). This observation highlights the influence of initial SOC on energy storage during the tests.

Notably, Case4, with the highest initial SOC, shows an approximately 20% reduction, while Cases 2 and 5 show an 18% reduction, and Case3 (with the lowest initial SOC) shows about a 0.3% reduction. Comparing the initial and final SOC levels in the WLTC and its inverted cycles, Case3 shows an increase of approximately 2% of its initial SOC at the end, while Case2 shows a reduction of about 15%. This finding highlights the critical role of the initial SOC in the overall energy balance and stability of the battery pack.

4.2. Detailed cell thermal performance

Experimental results indicate that on the same LIB cell, the temperature of the positive tab is higher than that of the negative tab, with a maximum difference of about 0.6 °C in Case1 [1,2,41]. This behavior is due to the thermomechanical properties of different materials used for the positive and negative tabs (aluminum and copper, respectively).

The maximum difference between the two mentioned positions occurs at the end of H2 in Cases 2 and 3, while in L1, Case3 shows a higher temperature difference due to a higher initial SOC. This trend is consistent in Cases 4 and 5.

An abnormality in $T^{+}_{1,06}$ was observed during WLTC in Section Section 3.5.1 (Fig. 12a), characterized by a temporary increase in temperature compared to neighboring cells. This irregularity could be attributed to two main causes: measurement errors or internal cell factors. First, measurement errors such as sensor misalignment, contact issues, or data acquisition inaccuracies may have contributed to the observed deviation. Repeating the test would likely eliminate this phenomenon. Second, the abnormality may reflect actual cell behavior (since positive tabs tend to have higher temperatures), potentially resulting from internal cell factors. Localized effects such as cell degradation, manufacturing variations, higher local current density, or higher internal resistance (polarization effects) could explain the higher readings. To ensure the validity of the thermal analysis, data from $T^{+}_{1,06}$ were excluded from pack-level calculations ($T_{max}(t)$, $T_{min}(t)$, $T_{avg}(t)$, $\Delta T(t)$, and T_{rise}) [31].

4.3. Detailed module thermal performance

The $T_{avg}(t)$ of Module1 in Case1 is higher than the pack T_{avg} during discharging periods (Ds) and the initial stages of Cs (high current portions). Module1 exhibits greater sensitivity to high currents, generating more heat and experiencing a faster temperature rise compared to the overall pack. This behavior is consistent in Cases 2, 3, 4, and 5, highlighting the complexity of the battery pack system and the need to study the thermal behavior of each module independently.

$T^{-}_{3,01}$ and $T^{-}_{2,12}$, measured on external cells close to the negative tabs, represent the $T_{min}(t)$ of the modules for Cases 2, 3, 4, and 5. Despite high initial temperatures in $T^{+}_{2,01}$ in Module2 in Case2, Case3, Case4, and Case5, as well as $T^{-}_{3,01}$ in Module3 in Case3, a decrease in their temperatures related to other cells is observed over the course

of the tests, eventually reaching one of the two lowest temperature points (Figs. 12, 13, 15, and 16). These effects arise from enhanced convective heat transfer, which improves cooling efficiency at the boundary surfaces of the module, aided by the ambient temperature.

In contrast, $T_{max}(t)$ is observed in the central cells of each module, illustrating the non-uniform temperature distribution within the LIB pack. This pattern highlights the complex dynamics of the system and underscores the necessity of evaluating temperature behavior across all modules in a battery pack.

4.4. Detailed pack thermal performance

In Case1, temperatures consistently increase during high current periods (237 A), including discharge cycles (Ds) and the beginning of each charging cycle (Fig. 11). The T_{max} during each cycle is observed at the end of the constant charging phase at 237 A, attributed to the increased movement of lithium ions.

In Cases 2, 3, 4, and 5, the time-averaged $T_{avg}(t)$ of the battery pack shows a gradually increase over the test, with the exception of the final L2 section in Case2 and Case3 (Fig. 14). The maximum temperature rises are observed during the H1 and M2 sections, highlighting these portions as the most thermally demanding for the battery pack.

The maximum ΔT of the pack remains below 4 °C across all cases, staying within the acceptable range for a LIB pack temperature difference [59–61]. Furthermore, the time-averaged $\Delta T(t)$ exhibits a gradual increase in Case2 and Case3, with the maximum value in M2, emphasizing the importance of an effective BTMS.

In Case5, with a higher initial $\Delta T(t)$ of 2.0 °C, the time-averaged $\Delta T(t)$ remains stable in the first two portions, L1 and M1, indicating the impact of initial $\Delta T(t)$ and energy equilibrium. This should be considered in future studies to estimate its influence on a pack in different scenarios.

In Case4 and Case5, the time-averaged $T_{avg}(t)$ of the pack increases by 9.1 °C, during the WLTC. In Case2 and Case3, the temperature rise is 10.5 °C and 11.4 °C, respectively, during the WLTC. This difference arises from the higher $T_{avg}(t)$ observed at the beginning of each cycle in Case3 (Figs. 12 and B.22), highlighting the importance of carefully considering initial SOC levels when evaluating and managing the thermal performance of the pack. In addition, the results show that higher initial temperatures lead to lower temperature rises during dynamic loads due to increased convective heat transfer.

4.5. Cooling system performance

As shown in Fig. 10, a transition occurs between $T_{max}(t)$ and $T_{min}(t)$ during the passive and active cooling phases. This shift can be attributed to two key factors. Firstly, in the absence of active liquid cooling during the initial cycles, heat transfer primarily relies on air convection. As a result, boundary cells on the pack's boundaries exhibit lower temperatures due to convective heat loss to the ambient environment, while the middle cells experience higher temperatures. Conversely, in cycles with active cooling (indicated by the blue background in Fig. 10), heat transfer to the liquid cooling medium becomes more significant. Since the middle cells generally have higher temperatures, the larger temperature gradient between these cells and the liquid medium leads to enhanced energy transfer from the middle cells to the liquid cooling system.

Similar to Case1, the liquid cooling system demonstrates a similar effect on the cell temperatures at the $T_{max}(t)$ points in both Case2 and Case3. As shown in Figs. 12 and 13, $T^{+}_{2,07}$ consistently exhibits higher temperatures throughout the test compared to other cells in the same module, except during the activation of the liquid cooling system (from the middle of M2 to the end of L2, indicated by the blue area). This behavior is primarily due to heat transfer between the cell bodies and the cooling medium. Consequently, the cooling system not only reduces the $T_{max}(t)$ of the pack in Case2 and Case3 but also contributes to a reduction in temperature non-uniformity, as reflected by the decrease in $\Delta T(t)$ (Fig. B.22 in Appendix B).

The findings reveal that during the low charge current period, the heat generated by the LIB pack is lower than the heat absorbed by the liquid cooling medium, resulting in a reduction in the pack's final temperature. As illustrated in Fig. 20b, the T_{rise} during the charging portions (Cs) decreases throughout the test. By the end of the test, the T_{rise} reaches its lowest value, as the energy absorption by the indirect liquid cooling system exceeds the heat generated by the battery cells.

The implementation of the indirect liquid cooling system in Case2 and Case3 maintains the $T_{max}(t)$ of the pack below 40.0 °C (blue area in figure B.22 in Appendix B), while in Case1, the T_{avg} of the pack exceeds this threshold despite the presence of the indirect cooling system. This is due to the constant high current discharging portion in Case1 for an extended period, producing significant energy and, consequently, higher temperatures. In real-world scenarios, similar to Case2 and Case3, the current cooling system maintains the pack temperature within the desired range. However, in high current scenarios, which are uncommon in typical driving styles but may occur, the BMS should adjust to the driving style accordingly to ensure a safer battery pack.

The findings highlight the cooling system's role in amplifying temperature behavior differences across the modules, emphasizing the importance of performing comprehensive temperature distribution tests throughout the battery pack (Figs. 11 and B.22 in B). In addition, the results reveal that even within the same battery pack, individual modules can exhibit variable thermal responses due to the applied cooling strategy. This behavior emphasizes the necessity of optimizing cooling strategies to minimize temperature differences across the pack.

The experimental and numerical results on a LIB cell show the influence and reliability of the cooling system during WLTC driving cycles in high-temperature periods. The results from Case2 and Case3 indicate that the liquid cooling system not only prevents the temperature of the battery cell from rising but also causes a temperature decrease of about 1% in both cases. This result contrasts with scenarios lacking a cooling system, where natural convection alone leads to a temperature increase of about 8%.

4.6. Model sensitivity to thermophysical parameters

The sensitivity analysis results presented in Fig. 4 enhance confidence in the numerical model's predictive capability and clarify the relative importance of the thermophysical parameters governing thermal behavior. Among the parameters evaluated, the specific heat and density of the LIB cell exhibit the greatest influence on the predicted T_{rise}, indicating their critical role in determining the thermal inertia of the system. These parameters are followed by the specific heat and density of the bottom plate, and the thermal conductivity of the LIB cell, which contribute to heat dissipation and storage. The convective heat transfer coefficient of air has a smaller, yet non-negligible, effect on thermal response under the passive conditions studied.

These findings underscore the importance of precise characterization of the thermal mass and conductive properties of the battery cell and associated structural components when modeling passive thermal behavior, particularly under transient loading conditions.

5. Conclusion

This study provides a comprehensive investigation on the thermal behavior of a 48 V LIB pack under real-world conditions for MHEV applications, focusing on typical operating temperatures. While most existing research focuses on high-voltage systems or steady-state scenarios, this work addresses the underexplored case of low-voltage packs under transient, real-world driving scenarios. The LIB pack is composed of three modules, each containing 12 prismatic NCM cells, to evaluate the effects of initial temperature, SOC, and temperature variations on the pack's thermal response. An indirect liquid cooling system was

activated at the bottom of the LIB modules when the pack temperature reached approximately 40 °C.

A combined experimental and numerical approach was employed to investigate the system's thermal behavior. A high number of thermocouples enabled high-resolution experimental evaluation of temperature distribution, while numerical simulations complemented the analysis by characterizing the thermal response under varying load conditions. In addition, a sensitivity analysis was conducted to identify the key thermophysical parameters influencing thermal predictions. The results highlighted the complex and nonlinear temperature dynamics across individual LIB cells, modules, and the entire pack, along with the influence of the indirect liquid cooling system on the pack's thermal behavior. Key findings include:

- The temperature at the positive tab was consistently higher than that at the negative tab within each cell, aligning with existing literature.
- An abnormal temperature reading in a specific internal battery cell was observed, suggesting potential external influences (such as sensor misalignment) or internal irregularities (such as manufacturing variation and local current concentration) in cell performance. This result underscores the importance of studying a high number of cells within the pack and carefully validating measurement systems.
- One of the modules demonstrated greater sensitivity to high currents, resulting in a faster temperature rise and enhanced heat generation. This observation could only be made by analyzing all the modules within the same LIB pack.
- Fully charging-discharging cycles showed a gradual increase in the average pack temperature and temperature difference during high-current portions. In the WLTC cases, the average pack temperature and temperature differences gradually increased over time, with certain sections applying the most significant thermal stress.
- In WLTC cases, decreasing the initial SOC increased the temperature rise, whereas increasing the initial temperature reduced the temperature rise. Increasing the initial temperature difference decreased the temperature difference rise in the cycle.
- During the passive cooling phase, external cells exhibited lower temperatures than the internal cells, due to more effective convective heat transfer.
- The implementation of an indirect liquid cooling system modified the temperature distribution within the pack, mitigating temperature rise in high constant current conditions and improving the pack's overall thermal performance.
- The liquid cooling system effectively maintained the maximum temperature below 40 °C during extreme thermal portions of the WLTC driving cycles. However, in the high-current charging and discharging case (Case1), temperatures reached approximately 46 °C. This behavior highlights the need for future research into alternative cooling systems that can regulate the temperature within the desired range according to varying load conditions.
- Sensitivity analysis showed that thermal mass-related properties of the LIB cell (specific heat and density) are the dominant factors influencing simulated temperature rise, showing the importance of accurate material characterization in thermal modeling.

Future research directions could expand on the findings of this study to further improve BTMS efficiency. Improving existing cooling methods, such as refining the cooling activation threshold and integrating localized control, may help reduce temperature gradients within the pack. In addition, developing alternative technologies such as PCMs are promising areas. PCMs offer advantages such as its ability to absorb and release heat over a wide temperature range, which can enhance temperature control in LIB packs. In addition, understanding the long-term impacts of dynamic load conditions, developing predictive models, and studying BTMS behavior under extreme ambient temperatures would provide valuable insights to further optimize LIB pack performance and longevity in real-world applications.

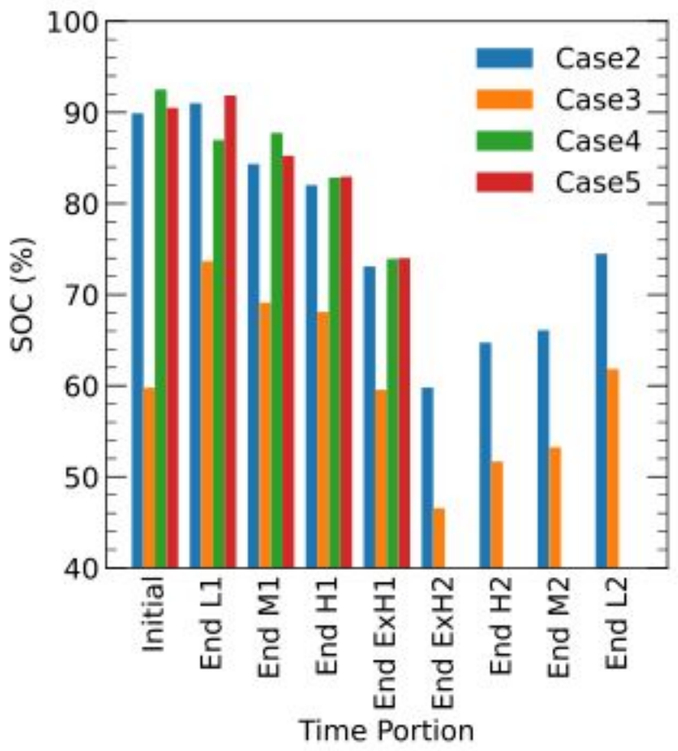

Fig. A.21. Final SOC comparison at each time portion in Case2, Case3, Case4, and Case5. L, M, H, and ExH represent low, medium, high, and extra-high speed sections.

CRediT authorship contribution statement

Hossein Darvish: Conceptualization, Methodology, Software, Validation, Formal analysis, Investigation, Resources, Data curation, Writing – original draft, Writing – review & editing, Visualization, Project administration. **Antonio Paolo Carlucci:** Conceptualization, Validation, Resources, Writing – review & editing, Supervision, Project administration. **Domenico Laforgia:** Validation, Resources, Supervision, Project administration.

Declaration of competing interest

The authors declare that they have no known competing financial interests or personal relationships that could have appeared to influence the work reported in this paper.

Appendix A. Average state of charge

This appendix presents the results of the SOC analysis conducted for four cases: Case2, Case3, Case4, and Case5. The SOC is a critical parameter in BMSs, representing the remaining energy capacity of the battery and requiring continuous monitoring and regulation. Fig. A.21 illustrates the final SOC levels recorded at the end of each time segment across the four cases. The x-axis denotes the specific time sections, while the y-axis depicts the SOC percentages.

Appendix B. Average temperature behavior for WLTC cases

This appendix presents an in-depth examination of the thermal behavior of the battery modules and pack during various test cycles. Temperature is a critical factor influencing battery performance, efficiency, and longevity, necessitating a thorough analysis of its fluctuations during operation. Figs. B.22 and B.23 illustrate the maximum, minimum, and average temperatures recorded in the modules for Case2, Case3, Case4, and Case5. Additionally, the average temperature and thermal gradient of the battery pack for these cases are depicted. This detailed visualization facilitates a comprehensive understanding of the thermal dynamics of the battery system during the test cycles.

Data availability

Data will be made available on request.

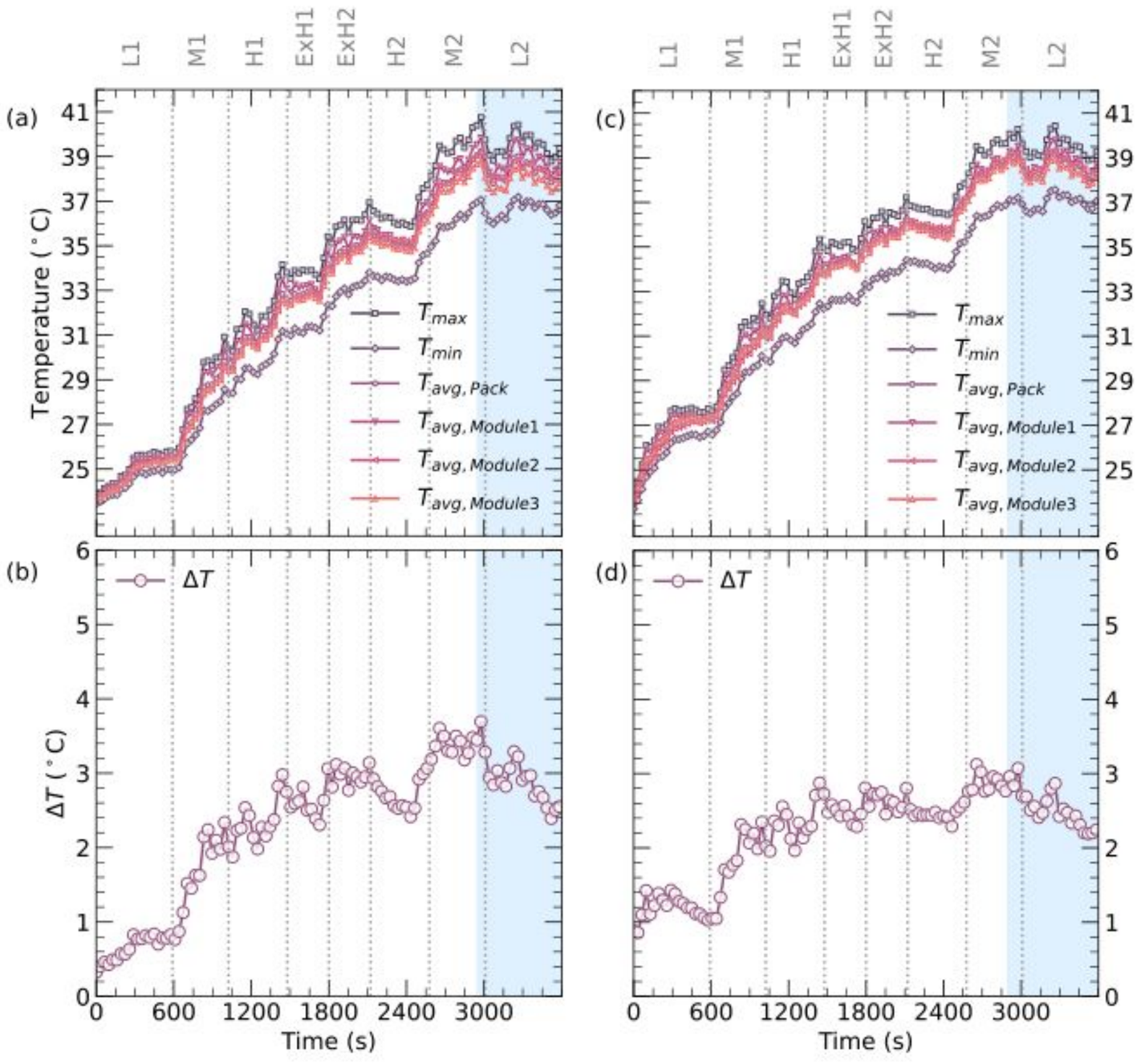

Fig. B.22. Average temperature of the pack ($T_{avg,Pack}$) and modules ($T_{avg,Module1}$, $T_{avg,Module2}$, and $T_{avg,Module3}$), as well as T_{max} and T_{min} of the pack for (a) Case2 and (c) Case3; the temperature difference (ΔT) behavior of the pack for (b) Case2 and (d) Case3. L, M, H, and ExH represent low, medium, high, and extra-high speed sections.

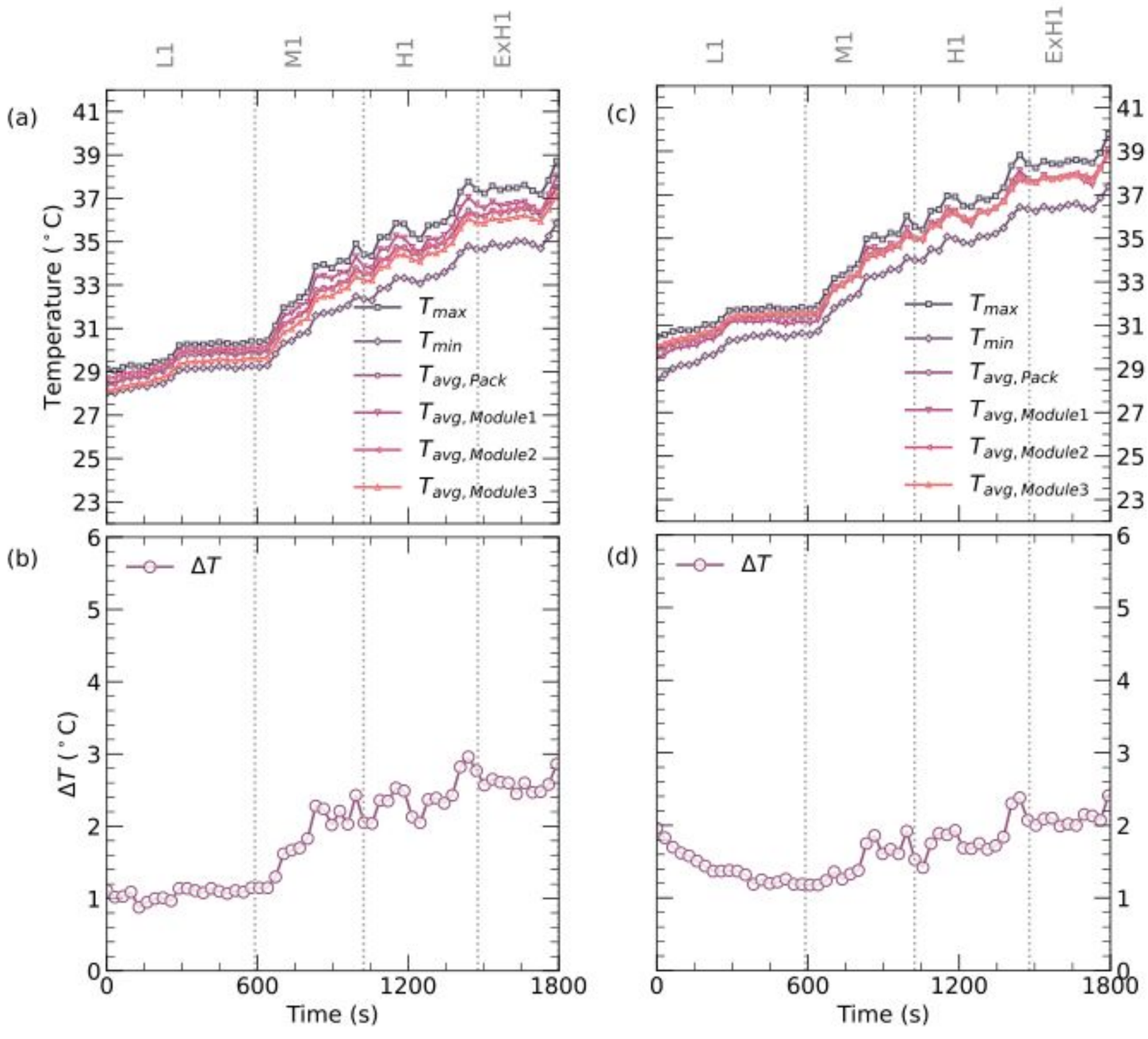

Fig. B.23. Average temperature of the pack ($T_{avg,Pack}$) and modules ($T_{avg,Module1}$, $T_{avg,Module2}$, and $T_{avg,Module3}$), as well as T_{max} and T_{min} of the pack for (a) Case4 and (c) Case5; the temperature difference (ΔT) behavior of the pack for (b) Case4 and (d) Case5. L, M, H, and ExH represent low, medium, high, and extra-high speed sections.

References

[1] N. Ghaeminezhad, Z. Wang, Q. Ouyang, A review on lithium-ion battery thermal management system techniques: A control-oriented analysis, Appl. Therm. Eng. 219 (2023) 119497.

[2] J. Jaguemont, F. Bardé, A critical review of lithium-ion battery safety testing and standards, Appl. Therm. Eng. 231 (2023) 121014.

[3] A. Emadi, Advanced Electric Drive Vehicles, CRC Press, 2014.

[4] A. Englisch, T. Pfund, D. Reitz, E. Simon, F. Kolb, Synthesis of various hybrid drive systems, in: Der Antrieb Von Morgen 2017: Hybride Und Elektrische Antriebssysteme 11. Internationale MTZ-Fachtagung Zukunftsantriebe, Springer, 2017, pp. 61–78.

[5] S. Lee, J. Cherry, M. Safoutin, J. McDonald, M. Olechiw, Modeling and validation of 48v mild hybrid lithium-ion battery pack, SAE Int. J. Altern. Powertrains 7 (3) (2018) 273–288.

[6] S. Lee, J. Cherry, M. Safoutin, A. Neam, J. McDonald, K. Newman, Modeling and Controls Development of 48 V Mild Hybrid Electric Vehicles, Tech. rep., SAE Technical Paper, 2018.

[7] A. Bhattacharjee, H. Saha, Development of an efficient thermal management system for vanadium redox flow battery under different charge-discharge conditions, Appl. Energy 230 (2018) 1182–1192.

[8] S. Dey, S. Mohon, P. Pisu, B. Ayalew, Sensor fault detection, isolation, and estimation in lithium-ion batteries, IEEE Trans. Control Syst. Technol. 24 (6) (2016) 2141–2149.

[9] M. Haji Akhoundzadeh, K. Raahemifar, S. Panchal, E. Samadani, E. Haghi, R. Fraser, M. Fowler, A conceptualized hydrail powertrain: A case study of the union pearson express route, World Electr. Veh. J. 10 (2) (2019) 32.

[10] H. Jouhara, N. Khordehgah, N. Serey, S. Almahmoud, S.P. Lester, D. Machen, L. Wrobel, Applications and thermal management of rechargeable batteries for industrial applications, Energy 170 (2019) 849–861.

[11] L. Wei, Z. Lu, F. Cao, L. Zhang, X. Yang, X. Yu, L. Jin, A comprehensive study on thermal conductivity of the lithium-ion battery, Int. J. Energy Res. 44 (12) (2020) 9466–9478.

[12] Z.-r. Li, G.-n. Liang, Y.-d. Ding, Q. Liao, X. Zhu, M. Cheng, Experimental study on the thermal management performance of lithium-ion battery with PCM combined with 3-D finned tube, Appl. Therm. Eng. 245 (2024) 122794.

[13] J. Lin, X. Liu, S. Li, C. Zhang, S. Yang, A review on recent progress, challenges and perspective of battery thermal management system, Int. J. Heat Mass Transfer 167 (2021) 120834.

[14] X. Zhu, Z. Wang, Y. Wang, H. Wang, C. Wang, L. Tong, M. Yi, Overcharge investigation of large format lithium-ion pouch cells with Li (Ni0. 6Co0. 2Mn0. 2) O2 cathode for electric vehicles: Thermal runaway features and safety management method, Energy 169 (2019) 868–880.

[15] M. Lu, X. Zhang, J. Ji, X. Xu, Y. Zhang, Research progress on power battery cooling technology for electric vehicles, J. Energy Storage 27 (2020) 101155.

[16] J. Liu, Q. Duan, M. Ma, C. Zhao, J. Sun, Q. Wang, Aging mechanisms and thermal stability of aged commercial 18650 lithium ion battery induced by slight overcharging cycling, J. Power Sources 445 (2020) 227263.

[17] A.A. Pesaran, Battery thermal models for hybrid vehicle simulations, J. Power Sources 110 (2) (2002) 377–382.

[18] Y. Liu, Y.G. Liao, M.-C. Lai, Lithium-ion polymer battery for 12-voltage applications: Experiment, modelling, and validation, Energies 13 (3) (2020) 638.

[19] J. Wang, Y. Yu, L. Song, Y. Yue, W. Zeng, W. Mei, Q. Wang, Thermal management performance and optimization of a novel system combining heat pipe and composite fin for prismatic lithium-ion batteries, Energy Convers. Manage. 302 (2024) 118106.

[20] S. Feng, S. Shan, C. Lai, J. Chen, X. Li, S. Mori, Multi-objective optimization on thermal performance and energy efficiency for battery module using gradient distributed tesla cold plate, Energy Convers. Manage. 308 (2024) 118383.

[21] T. Liu, C. Tao, X. Wang, Cooling control effect of water mist on thermal runaway propagation in lithium ion battery modules, Appl. Energy 267 (2020) 115087.

[22] T. Liu, Y. Liu, X. Wang, X. Kong, G. Li, Cooling control of thermally-induced thermal runaway in 18,650 lithium ion battery with water mist, Energy Convers. Manage. 199 (2019) 111969.

[23] S.A. Khan, I. Hussain, A.K. Thakur, S. Yu, K.T. Lau, S. He, K. Dong, J. Chen, L. Xiangrong, M. Ahmad, et al., Advancements in battery thermal management system for fast charging/discharging applications, Energy Storage Mater. (2023) 103144.

[24] P.R. Tete, M.M. Gupta, S.S. Joshi, Developments in battery thermal management systems for electric vehicles: A technical review, J. Energy Storage 35 (2021) 102255.

[25] R. Kumar, S. Chavan, Coupled electro-chemical and thermal modeling for cylindrical lithium-ion batteries, Tech. rep., SAE Technical Paper, 2021.

[26] C. Lin, Y. Liu, J. Zhang, L. Han, B. Fan, Y. Luo, F. Wang, Thermal uniformity of pouch-type lithium ion batteries with NCM cathode materials under different operating conditions, Tech. rep., SAE Technical Paper, 2019.

[27] J. Hall, S. Borman, B. Hibberd, M. Bassett, S. Reader, M. Berger, 48 V high-power battery pack for mild-hybrid electric powertrains, SAE Int. J. Adv. Curr. Pr. Mobil. 2 (2020-01-0441) (2020) 1893–1904.

[28] P.G. Anselma, F. Miretti, E. Spessa, Impact of predictive battery thermal management for a 48V hybrid electric vehicle, in: 2022 IEEE Transportation Electrification Conference & Expo, ITEC, IEEE, 2022, pp. 267–272.

[29] U. Han, H. Kang, J. Song, J. Oh, H. Lee, Development of dynamic battery thermal model integrated with driving cycles for EV applications, Energy Convers. Manage. 250 (2021) 114882.

[30] A.P. Carlucci, H. Darvish, D. Laforgia, Detailed thermal characterization on a 48V lithium-ion battery pack during charge-discharge cycles, Tech. rep., SAE Technical Paper, 2023.

[31] A.P. Carlucci, H. Darvish, D. Laforgia, Thermal performance of a 48V prismatic lithium-ion battery pack under WLTC driving cycles with a liquid cooling system, SAE Int. J. Adv. Curr. Pr. Mobil. 6 (2023-24-0152) (2023) 1868–1882.

[32] A.P. Carlucci, H. Darvish, D. Laforgia, Thermal mapping analysis of a 48V prismatic lithium-ion battery pack with active and passive cooling, in: Journal of Physics: Conference Series, 2648, IOP Publishing, 2023, 012098.

[33] K. Nandagopal, R. Sok, K. Kishida, T. Otake, J. Kusaka, Measured thermal performances at brick and module levels in a battery pack of a mid-size electric vehicle under WLTC and FTP driving cycles, Tech. rep., SAE Technical Paper, 2024.

[34] J. Zeng, S. Feng, C. Lai, J. Song, L. Fu, H. Chen, S. Deng, T. Gao, Prediction on thermal performance of refrigerant-based battery thermal management system for a HEV battery pack, Int. J. Heat Mass Transfer 201 (2023) 123657.

[35] Y. Chen, Y. Kang, Y. Zhao, L. Wang, J. Liu, Y. Li, Z. Liang, X. He, X. Li, N. Tavajohi, et al., A review of lithium-ion battery safety concerns: The issues, strategies, and testing standards, J. Energy Chem. 59 (2021) 83–99.

[36] R. Schröder, M. Aydemir, G. Seliger, Comparatively assessing different shapes of lithium-ion battery cells, Procedia Manuf. 8 (2017) 104–111.

[37] P.N. Halimah, S. Rahardian, B.A. Budiman, Battery cells for electric vehicles, Int. J. Sustain. Transp. Technol. 2 (2) (2019) 54–57.

[38] W. Li, Y. Xia, G. Chen, E. Sahraei, Comparative study of mechanical-electrical-thermal responses of pouch, cylindrical, and prismatic lithium-ion cells under mechanical abuse, Sci. China Technol. Sci. 61 (2018) 1472–1482.

[39] J. Jürgens, This is Why NCM is the preferable cathode material for Li-ion batteries, LG Energy Solution Blog (2019) Online: https://lghomebatteryblog.eu/this-is-why-ncm-is-the-preferable-cathode-material-for-li-ion-batteries/.

[40] H.C. Hesse, M. Schimpe, D. Kucevic, A. Jossen, Lithium-ion battery storage for the grid—A review of stationary battery storage system design tailored for applications in modern power grids, Energies 10 (12) (2017) 2107.

[41] P. Lyu, X. Liu, C. Liu, Z. Rao, Experimental and modeling investigation on thermal risk evaluation of tabs for pouch-type lithium-ion battery and the relevant heat rejection strategies, Int. J. Heat Mass Transfer 202 (2023) 123770.

[42] U.S. Kim, C.B. Shin, C.-S. Kim, Modeling for the scale-up of a lithium-ion polymer battery, J. Power Sources 189 (1) (2009) 841–846.

[43] B. Heidarshenas, A. Aghaei, A.H. Zamani, Y. Yuan, Comparison of different cooling techniques for a lithium-ion battery at various discharge rates using electrochemical thermal modeling, Appl. Therm. Eng. 258 (2025) 124596.

[44] M. Hussain, M.K. Khan, M. Pathak, Thermal analysis of phase change material encapsulated li-ion battery pack using multi-scale multi-dimensional framework, J. Energy Storage 65 (2023) 107290.

[45] A. Fluent, et al., Ansys fluent theory guide, Ansys Inc., USA 15317 (2011) 724–746.

[46] Y. Morimoto, Y. Ohya, K. Abe, T. Yoshida, H. Morimoto, Computer simulation of the discharge reaction in lead-acid batteries, J. Electrochem. Soc. 135 (2) (1988) 293.

[47] K.H. Kwon, C.B. Shin, T.H. Kang, C.-S. Kim, A two-dimensional modeling of a lithium-polymer battery, J. Power Sources 163 (1) (2006) 151–157.

[48] V.-T. Ho, K. Chang, S.W. Lee, S.H. Kim, Transient thermal analysis of a li-ion battery module for electric cars based on various cooling fan arrangements, Energies 13 (9) (2020) 2387.

[49] J. Holman, J. Boggs, Heat transfer to Freon 12 near the critical state in a natural-circulation loop, ASME J. Heat Mass Transf. 82 (1960) 221–226.

[50] M. Akbarzadeh, T. Kalogiannis, J. Jaguemont, J. He, L. Jin, M. Berecibar, J. Van Mierlo, Thermal modeling of a high-energy prismatic lithium-ion battery cell and module based on a new thermal characterization methodology, J. Energy Storage 32 (2020) 101707.

[51] M. Akbarzadeh, T. Kalogiannis, J. Jaguemont, L. Jin, H. Behi, D. Karimi, H. Beheshti, J. Van Mierlo, M. Berecibar, A comparative study between air cooling and liquid cooling thermal management systems for a high-energy lithium-ion battery module, Appl. Therm. Eng. 198 (2021) 117503.

[52] C. Li, Y. Ding, Z. Zhou, Y. Jin, X. Ren, C. Cao, H. Hu, Parameter optimization and sensitivity analysis of a lithium-ion battery thermal management system integrated with composite phase change material, Appl. Therm. Eng. 228 (2023) 120530.

[53] M. Song, S.-Y. Choe, Parameter sensitivity analysis of a reduced-order electrochemical-thermal model for heat generation rate of lithium-ion batteries, Appl. Energy 305 (2022) 117920.

[54] H. Chen, G. Wei, L. Xu, X. Du, Performance study on a novel hybrid thermal management system for cylindrical lithium-ion battery pack based on liquid cooling and PCM, Appl. Therm. Eng. 271 (2025) 126392.

[55] X. Lai, S. Wang, S. Ma, J. Xie, Y. Zheng, Parameter sensitivity analysis and simplification of equivalent circuit model for the state of charge of lithium-ion batteries, Electrochim. Acta 330 (2020) 135239.
[56] M.A. Hannan, M.H. Lipu, A. Hussain, A. Mohamed, A review of lithium-ion battery state of charge estimation and management system in electric vehicle applications: Challenges and recommendations, Renew. Sustain. Energy Rev. 78 (2017) 834–854.
[57] G.L. Plett, Battery Management Systems, Volume II: Equivalent-Circuit Methods, Artech House, 2015.
[58] T. Heenan, I. Mombrini, A. Llewellyn, S. Checchia, C. Tan, M. Johnson, A. Jnawali, G. Garbarino, R. Jervis, D. Brett, et al., Mapping internal temperatures during high-rate battery applications, Nature 617 (7961) (2023) 507–512.
[59] M. Hu, J. Wang, C. Fu, D. Qin, S. Xie, Study on cycle-life prediction model of lithium-ion battery for electric vehicles, Int. J. Electrochem. Sci. 11 (1) (2016) 577–589.
[60] W. Liu, Z. Jia, Y. Luo, W. Xie, T. Deng, Experimental investigation on thermal management of cylindrical Li-ion battery pack based on vapor chamber combined with fin structure, Appl. Therm. Eng. 162 (2019) 114272.
[61] R. Kizilel, R. Sabbah, J.R. Selman, S. Al-Hallaj, An alternative cooling system to enhance the safety of Li-ion battery packs, J. Power Sources 194 (2) (2009) 1105–1112.